Water Resources Research

Key Points:

- Yellowstone Lake sediments respond to hydrodynamically induced bottom water temperature variations and, in thermal areas, hydrothermal processes
- Hydrodynamic processes drive hypolentic flow in the upper ~20 cm of the lakefloor sediments at deep (>80 m) water depths
- Hydrothermal processes generate fingered discharge and short wavelength convection in the Deep Hole thermal area sediments

Spectral Analysis of Vertical Temperature Profile Time-Series Data in Yellowstone Lake Sediments

Robert A. Sohn[1] and Robert N. Harris[2]

[1]Geology and Geophysics Department, Woods Hole Oceanographic Institution, Woods Hole, MA, USA, [2]College of Earth, Ocean, and Atmospheric Sciences, Oregon State University, Corvallis, OR, USA

Abstract We use yearlong vertical temperature profile time-series (seven thermistors at evenly spaced depth intervals from 10 to 70 cm) from five sites in and around the Deep Hole thermal area, southeast of Stevenson Island, Yellowstone Lake, to investigate heat and mass fluxes across the lake floor. The records demonstrate that thermal gradients in surficial sediments are modulated by a rich spectrum of bottom water temperature variations generated by hydrodynamic processes, and that sites inside the thermal area also respond to hydrothermal variations. We develop and implement a new method for estimating the sediment effective thermal diffusivity and pore fluid vertical flow rate that exploits the full spectrum of observed temperature variations to generate the parameter estimates, uncertainties, and metrics to assess statistical significance. Sediments at sites outside thermal areas have gradients of ~7.5°C/m, in situ thermal diffusivities of ~1.6×10^{-7} m^2/s consistent with highly porous (80–90%) siliceous sediments, and experience hypolentic flow in the upper ~20 cm. Sites inside the Deep Hole thermal area exhibit considerable spatial and temporal variability, with gradients of 1–32°C/m, and higher thermal diffusivities of ~2–12×10^{-7} m^2/s, consistent with hydrothermal alteration of biogenic silica to clays, quartz, and pyrite. Upward pore fluid flow at these sites is observed across multiple depth intervals, with maximum values of ~3 cm/day. The observed spatial and temporal variability within the thermal area is consistent with upward finger flow combined with short wavelength convection within the porous sediments above a steam reservoir.

1. Introduction

Vertical temperature profile (VTP) data provide a means to quantify heat and mass fluxes across the ground surface in a variety of geological and ecological environments. VTP measurements have long been used to constrain heat fluxes across the Earth's solid surface, and these studies have played an important role in our understanding of the Earth's thermal history (e.g., Bullard, 1945; Kelvin, 1863). VTP measurements can also be used to estimate fluid fluxes. Stallman (1965) and Bredehoeft and Papadopulos (1965) described how temperature-depth profiles in a steady state, porous medium can be used to constrain vertical fluid flux rates. Although this method has been applied in a variety of hydrologic environments (e.g., Cartwright, 1970; Ferguson et al., 2003; Sorey, 1971; Taniguchi, 1993), the steady state thermal assumption is not always satisfied in natural systems. Suzuki (1960) and Stallman (1965) demonstrated that fluid flux rates can be constrained using time-series VTP data if the ground surface interface experiences periodic temperature variations. These studies showed that fluid flow modifies the rate and amplitude decay of downward diffusing thermal signals such that the amplitude ratio and phase lag between vertically offset thermistor pairs can be used to constrain fluid flux rates. Because many natural systems experience periodic temperature variations, the Stallman (1965) method has been widely applied to diverse hydrologic environments, including streams, rivers, coastal oceans, and deep-sea hydrothermal fields (e.g., Anderson, 2005; Constantz et al., 2008; Goto et al., 2005; Hatch et al., 2006; Wilson et al., 2016).

Fluid fluxes into (infiltration), or out of (seepage), sediments have important implications for the transport of solutes and nutrients in many hydrologic systems, including streams (e.g., Bohlke et al., 2009; Fuller & Harvey, 2000; Mulholland et al., 2001) and oceans (e.g., Billerbeck et al., 2006; Burnett et al., 2003; Precht & Huettel, 2004). Ground water fluxes can be important for understanding water balances and nutrient fluxes in lakes (e.g., Hayashi & Rosenberry, 2002; Mortimer, 1941; Sierszen et al., 2014; Winter 1981, 1983, 1999), and in some cases represent the dominant mode of gain or loss (e.g., Gurrieri & Furniss, 2004; Rosenberry, 2000; Stets et al., 2010). However, lacustrine studies often disregard ground water fluxes, including

hyporheic exchange (Meinikmann et al., 2013; Rosenberry et al., 2015) due to a variety of factors, including the technical and logistical difficulties associated with acquiring the necessary data (Rosenberry et al., 2015).

Recently, however, groundwater fluxes in lacustrine systems have gained renewed attention, due at least in part to concerns regarding eutrophication (e.g., Gelbrecht et al., 2005; Lewandowski et al., 2015). Thermal methods for constraining groundwater fluxes are appealing due to their simplicity, durability, and cost, relative to other methods (e.g., seepage meters, piezometers, tracer injection experiments), and although they are typically based on one-dimensional solutions to the heat transport equation, they can provide useful estimates even when more complex two-dimensional and three-dimensional flow patterns exist (e.g., Bhaskar et al., 2012; Lautz, 2010). The advent of fiber-optic distributed thermal sensing has stimulated several studies using heat as a tracer to constrain groundwater fluxes in lakes (e.g., Blume et al., 2013; Sebok et al., 2013; Tristram et al., 2015), but simpler point measurements have also proven effective (Meinikmann et al., 2013).

Most thermal studies of lacustrine groundwater flux to-date have assumed constant bottom water temperatures, and although most lakes are deep enough such that temperature variations at the lake surface will not diffuse to the lake floor, meteorological processes can generate a wide range of hydrodynamic behaviors in lakes, including barotropic and baroclinic seiching, basin-scale currents, and convective overturning (e.g., Austin, 2013; Csanady, 1967; Rueda et al., 2003; Wuest & Lorke, 2003). These dynamic processes transfer energy from the lake surface to the lake floor, providing a means to modify the lake floor interface temperature at a variety of time scales. These considerations motivate the acquisition of VTP time-series data in lacustrine settings to investigate the use of hydrodynamic thermal variations to constrain groundwater fluxes.

We present VTP time-series data that we acquired from the deep (82–113 m) floor of Yellowstone Lake over two consecutive annual periods in order to investigate how hydrothermal processes affect heat and mass flow across the lake floor. We find that hydrodynamic processes generate sediment temperature variations that are coherent between vertically offset thermistors over a broad range of frequencies in all records. In addition, we find that hydrothermal processes generate coherent thermal signals at sites inside the hydrothermal area. We develop and utilize a method that exploits the broad spectrum of coherent thermal variations to generate robust estimates of both the effective thermal diffusivity of the sediments and the pore fluid vertical fluid velocity at our measurement sites. We use our results to constrain heat and mass fluxes across deep portions the lake bed, the thermophysical properties of the lake floor sediments, and the nature of fluid flow in the thermal area sediments.

2. Field Site and Time-Series Data

Yellowstone Lake (44°28′N, 110°22′W) is a large (~341 km^2, ~120 m max depth) alpine lake (2,357 m altitude) located in Yellowstone National Park in northwestern Wyoming, USA. The lake hosts a unique ecosystem in a highly protected landscape (Koel et al., 2019). Hydrothermal discharge through the lake floor modifies the lake's shape and composition (Balistrieri et al., 2007; Morgan et al., 2003), generates water column plumes (Sohn et al., 2019), and provides habitat for chemosynthetic biological communities (Clingenpeel et al., 2011; Kan et al., 2011; Klump et al., 1988). The flux of volcanic/hydrothermal heat into the lake is focused in the northern portion, which lies inside the ~640 ka Yellowstone caldera (Morgan et al., 1977, 2003), but the associated mass fluxes are poorly understood, and the time-space patterns associated with fluid discharge and recharge at individual hydrothermal fields are unknown.

Hydrothermal discharge can generate characteristic pockmarks with depths of up to ~20 m in the lacustrine sediments due to some combination of dissolution, settling, and particle removal, which makes sites of past or present discharge relatively easy to discern in bathymetric maps (Morgan et al., 2003). Remotely Operated Vehicle (ROV) dives have established the presence of active discharge in several regions, including a site informally known as the "Deep Hole" to the south/southeast of Stevenson Island (Figure 1). The Deep Hole thermal area is a vapor-dominated system with a total heat output of ~28 MW (Sohn et al., 2019), discharging volatile-rich (CO_2, H_2S), acidic (in situ pH of 4.2–4.5), and reducing (−0.2 to −0.3 V) fluids, reflecting a mixture of a volatile-bearing steam condensate with oxygenated, neutral pH lake water (Fowler, Tan, et al., 2019). The hydrothermal fluids locally alter the siliceous lacustrine sediments via sulfide
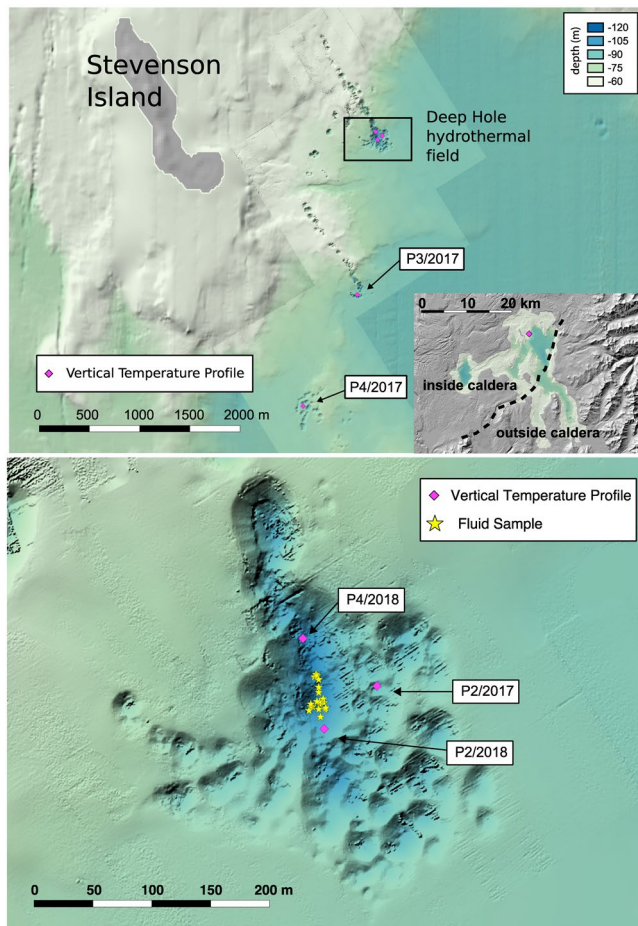
Figure 1. Top panel: Location of VTP deployments. Inset: Map of Yellowstone Lake. Magenta diamond indicates location of Deep Hole hydrothermal field. Dashed black line shows boundary of 640 ka Yellowstone caldera. Bottom panel: Zoom view of the Deep Hole hydrothermal field, located to the east of Stevenson Island, as indicated by boxed region in top panel. Yellow stars indicate location of active venting sites sampled and described in Fowler, Tan, et al. (2019).

mineralization into pyrite-bearing kaolinite, with boehmite and trace pyrrhotite, at the discharge sites (Fowler, Liu, et al., 2019).

While the heat and mass fluxes associated with hydrothermal discharge into Yellowstone Lake have been investigated (Balistrieri et al., 2007; Sohn et al., 2019), the nature of pore fluid flow in the lake floor sediments, including groundwater fluxes and hypolentic exchanges, has not been studied. From 2016 to 2018, the Hydrothermal Dynamics of Yellowstone Lake (HD-YLAKE) project deployed a variety of geochemical and geophysical monitoring instrumentation on the lake floor, including a focus site at the Deep Hole thermal field (Sohn et al., 2017). As part of this effort, we acquired VTPs from the lake floor, using custom-built probes that are 1-m long, 2.5-cm in diameter, and contain seven thermistors (0.05°C resolution) each with a 10-cm interelement spacing. The top thermistor is 10-cm beneath the top of the probe, and thus was positioned approximately 10 cm below the lake floor interface, while the bottom thermistor was 60 cm below the top thermistor, and was thus approximately 70 cm below the lake floor. Temperature was recorded every 15 min using an autonomous data logger.

We deployed these instruments using the remotely operated vehicle *Yogi* (http://engineeringfordiscovery.org/technology/rov-yogi/) at seven, deep water (>80 m) sites in the lake over the course of two sequential field seasons during the summers of 2016 and 2017. Five of these seven deployments returned data, providing yearlong, continuous records from August to August. Two records were acquired inside the Deep Hole thermal field, one was acquired from the edge of the thermal field, and two were acquired from the margins of inactive pockmark fields further south (Figure 1). Note that the data are radiolabeled according to the year each probe was recovered. The characteristics of each site and data record are listed in Table 1. The time-series data are shown in Figures 2 and 3 for the 2016–2017 and 2017–2018 deployments, respectively.

Sediment temperatures at most of the sites exhibit a temporal evolution that corresponds to the annual bottom water temperature (BWT) cycle of dimictic Yellowstone Lake (Benson, 1961). This pattern is characterized by a steady temperature increase during the Summer and Fall months, followed by a relatively abrupt decrease in the December-January interval associated with convective overturning of the lake prior to ice-over. BWTs slowly increase during the ice-covered interval, which lasts 4–5 months, before a second overturning event, typically in May, temporarily decreases BWTs prior to the return of summer warming. This pattern characterizes the temporal trends in the 2017 data (Figure 2), but is overprinted to varying degrees in the

Table 1
VTP Measurement Site Information

Site	Longitude (°W)	Latitude (°N)	Depth (m)	Record length (ddd:hh:mm)	Mean gradient (°C/m)	Mean heat flux ± std.dev (W/m^2)	Notes
P2/2017	110.35593	44.51085	92	350:04:29	1.67	1.25 ± 0.51	Edge of active thermal field
P3/2017	110.35907	44.49662	92	348:19:17	7.41	5.56 ± 0.48	Edge of inactive pockmark field
P4/2017	110.36585	44.48664	82	347:23:38	7.56	5.67 ± 0.48	Edge of inactive pockmark field
P2/2018	110.35653	44.51052	101	351:21:32	5.78	5.78 ± 0.48	Inside active thermal field
P4/2018	110.35677	44.51121	113	221:03:45	12.84	12.84 ± 3.99	Inside active thermal field

All records sampled at 15 min intervals on seven thermistors with 10 cm interelement spacing.
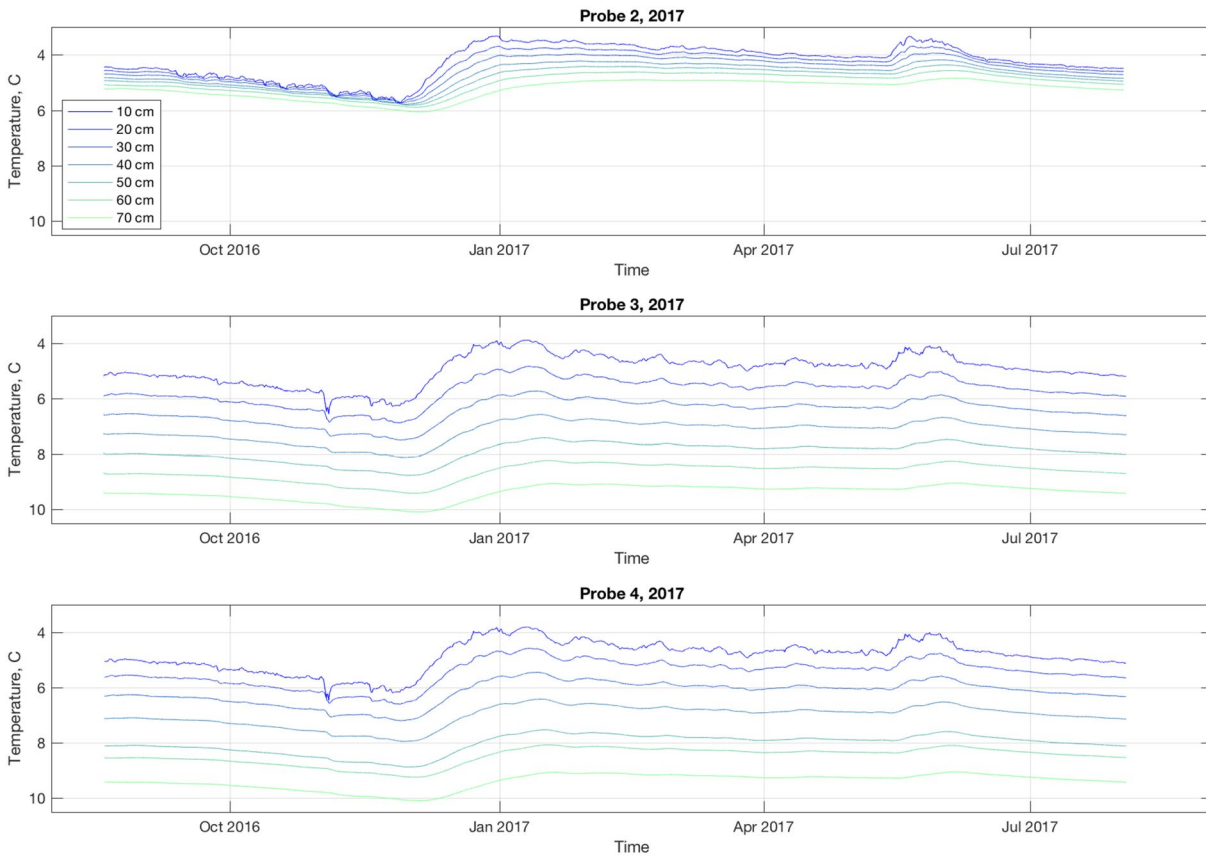
Figure 2. VTP time-series data acquired from 2016 to 2017. Thermistor depth is shown in the legend in the top panel.

2018 data acquired from the Deep Hole thermal site (Figure 3), presumably due to the influence of hydrothermal processes.

3. Methods

3.1. Average Thermal Gradients

We calculated the average vertical thermal gradient measured at each 15 min sample interval for each record by quantifying the temperature difference between the top thermistor (10 cm depth) and the bottom thermistor (70 cm depth) and dividing by the 60 cm depth offset ($\nabla T = dT / dz$, where T is temperature and z is depth). This allows us to generate time-series records of the average thermal gradient for each measurement site.

3.2. Spectral Analyses

Power spectra were estimated for the temperature time-series data using the multitaper method (Thomson, 1982) with adaptive weighting (Percival & Walden, 1993) and a time-half bandwidth product of five. Each record was first detrended to remove the mean value, and spectral estimates were then generated using the entire yearlong time-series, except for the Probe 4/2018 record, which was ~7 months long. Cross-spectral estimates of the coherency, amplitude ratio, and phase lag between adjacent thermistor pairs on the VTP probes were made using the same method. We then extracted a subset of statistically independent cross-spectral estimates to account for the effects of leakage, which is an artifact the window functions
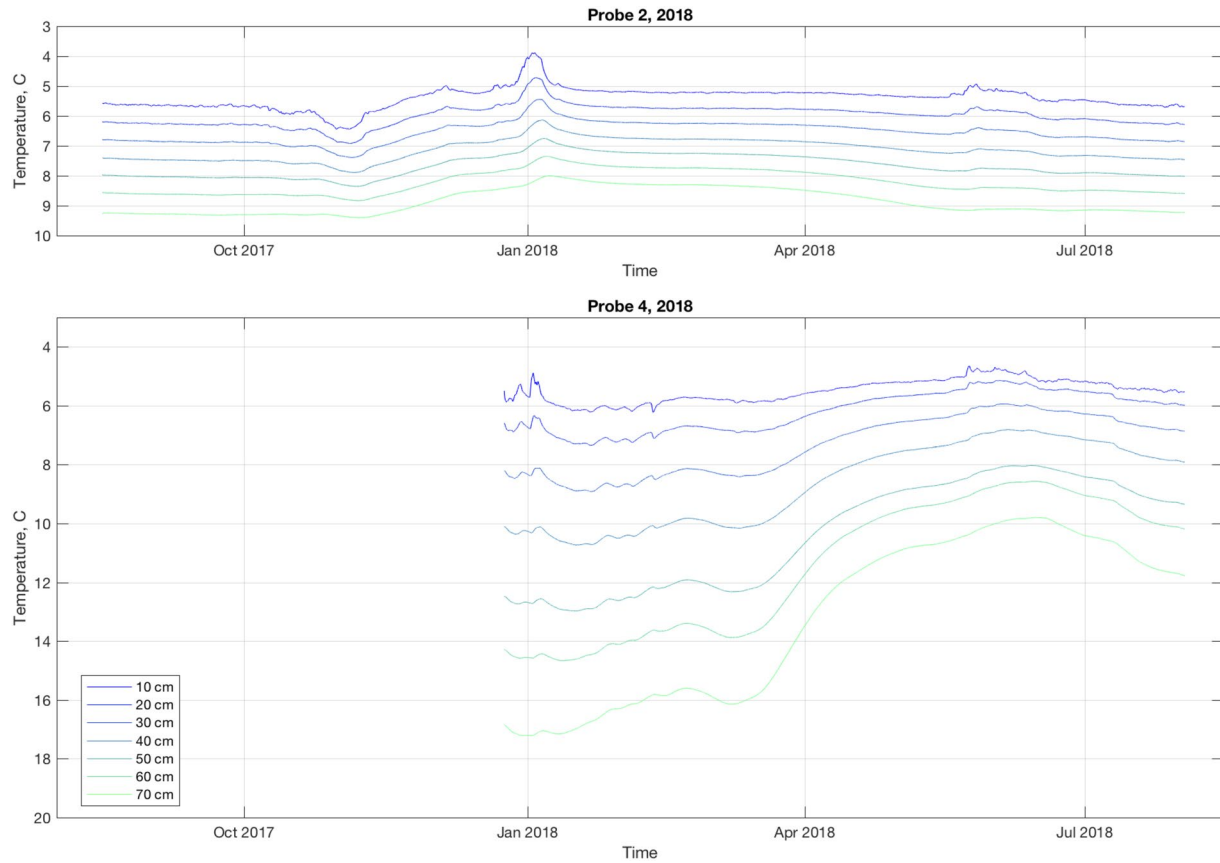
Figure 3. VTP time-series data acquired from 2017 to 2018. Note that Probe 4 did not start logging data until late December 2017, due to technical issues, and that the *y* axis in bottom panel is expanded to allow for direct visual comparison of gradients.

used to taper the data. The equations used to generate the cross-spectral estimates and extract values for statistically independent frequencies are provided in the supporting information S1.

3.3. Amplitude Ratio and Phase Lag

VTP time-series data provide a means to estimate the effective thermal diffusivity and vertical pore fluid velocity of the sediments (e.g., Suzuki, 1960; Stallman, 1965). The simplest scenario involves the purely vertical flow of heat and mass in a semi-infinite half-space (in the region $z \geq 0$, z is depth, positive downwards) utilizing the one-dimensional advection-diffusion equation

$$\frac{\partial T}{\partial t} = \kappa_e \frac{\partial^2 T}{\partial z^2} - \frac{n v_f}{\gamma} \frac{\partial T}{\partial z},$$

(1)

where T is temperature, t is time, κ_e is effective thermal diffusivity, n is porosity, v_f is fluid vertical velocity, and $\gamma = \rho_m c_m / \rho_f c_f$ is the ratio of heat capacities (subscript m for saturated sediment matrix, subscript f for fluid, ρ is density, and c is specific heat).

Assuming that: (1) the fluid velocity is constant, (2) the fluid temperature is equal to the matrix temperature at any point on the vertical axis at all times, and (3) the temperature at $z = \infty$ is not influenced by the surface variations, it has been shown that a periodic temperature perturbation applied to the surface of the half-space generates a downward propagating thermal signal where the amplitude ratio, Ar, and phase lag, ϕ, between two points offset by a vertical distance, Δz, is given by
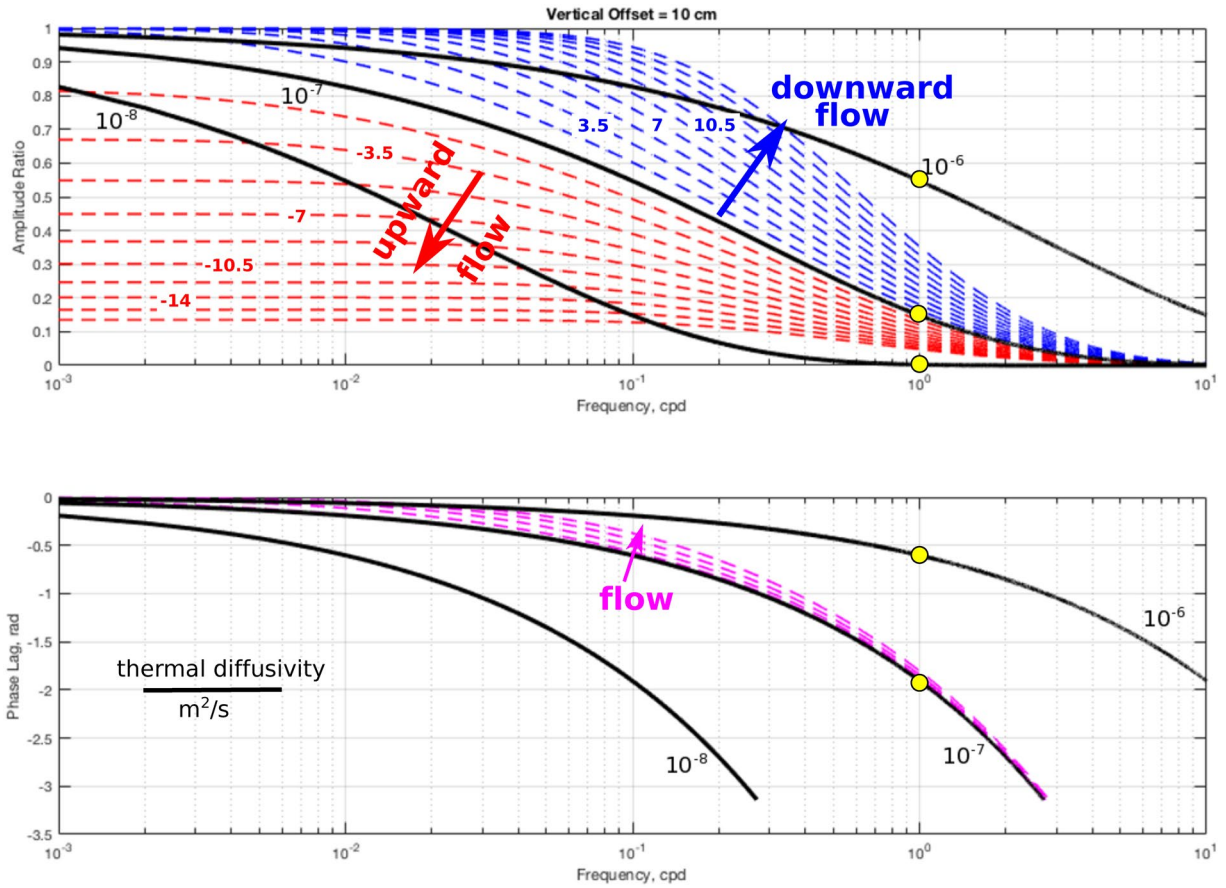
Figure 4. Relationship between amplitude ratio (*Ar*, top panel) and phase lag (φ, bottom panel) with respect to angular frequency (ω), effective thermal diffusivity (κ_e), and thermal front velocity (*v*) for a nominal vertical offset distance (Δz) of 10 cm. Black lines represent diffusion-only (*v* = 0) relationships for effective thermal diffusivities of 10^{-6}, 10^{-7}, and 10^{-8} m²/s. Dashed lines represent relationships for an effective diffusivity of 10^{-7} m²/s with downward (i.e., infiltration, blue lines in top panel) and upward (i.e., seepage, red lines in top panel) thermal front velocities in increments of 1.75 cm/day (every other increment radiolabeled). In this reference frame upward velocities are negative. Magenta dashed lines in bottom panel represent the same range of thermal front velocities (±14 cm/day) in increments of (3.5 cm/day). The yellow dots indicate the values corresponding to the diurnal frequency for diffusion-only scenarios.

$$Ar = exp\left(-\frac{\Delta z}{2\kappa_e}\left(\sqrt{\frac{\alpha + v^2}{2}} - v\right)\right), \tag{2}$$

and

$$\phi = \frac{\Delta z}{2\kappa_e}\left(\sqrt{\frac{\alpha - v^2}{2}}\right), \tag{3}$$

respectively, where $v = v_f / \gamma$ is the penetration rate of the thermal front, $\alpha = \sqrt{v^4 + \left(4\kappa_e\omega\right)^2}$, and ω is angular frequency (Goto et al., 2005; Hatch et al., 2006).

Functionally, Equations 2 and 3 act as a low-pass filter that preferentially attentuates and delays the downward propagation of high-frequency signals, where the rate of attenuation is primarily determined by κ_e (Figure 4). Smaller values of κ_e produce faster attenuation rates and larger phase lags. For example, if there is no fluid flow, then at a depth of 10 cm, a diurnal signal, regardless of its amplitude, is completely attenuated in a medium with $\kappa_e = 10^{-8}$ m²/s, but retains ~16% of its original amplitude in a medium with $\kappa_e = 10^{-7}$ m²/s, and ~55% of its original amplitude in a medium with $\kappa_e = 10^{-6}$ m²/s. Fluid flow does not

have much effect on the phase lag, but it impacts the amplitude ratio in complicated ways that depend on frequency. Upward flow always reduces the amplitude ratio, and downward flow always increases the amplitude ratio, relative to diffusion-only scenarios, but the magnitude of the effect depends on both κ_e and frequency, as well as the flow rate. In contrast, vertical fluid flow always reduces the phase lag, regardless of flow direction, by a relatively small amount. As we describe below, the complex and nonlinear relationships between amplitude ratio and phase lag with respect to frequency, effective thermal diffusivity, and vertical fluid flow rate in a porous medium have important implications for estimating κ_e and v_f using Equations 2 and 3.

3.4. Multifrequency Parameter Estimation Method

Equations 2 and 3 provide a means for estimating κ_e and v on the basis of Ar and ϕ estimates. At any given frequency, ω, the unknown model parameters (κ_e, v) are constrained by two observations (Ar, ϕ). Most previous methods put forward to estimate the model parameters using these equations focus solely on a single frequency—typically the diurnal frequency, but annual frequencies have also been used (Bartolino & Niswonger, 1999; Taniguchi, 1993). The most common approach has been to assume a value for the thermal diffusivity, and then estimate the velocity term using the diurnal amplitude ratio (e.g., Hatch et al., 2006; Keery et al., 2007). However, Luce et al. (2013) showed that it is not necessary to assume values for the thermal diffusivity, and more accurate results may be obtained by using both Ar and ϕ to estimate κ_e and v.

Although many hydrologic environments experience thermal variations at diurnal frequencies, there is no formal requirement to restrict the inverse procedure to a single frequency. Indeed, restricting the inversion to a single frequency can amount to discarding useful data since the Fourier spectrum of a real signal invariably contains power at many frequencies. The governing equations (Equations 2 and 3) are completely general with respect to frequency, and can be expressed as a spectral operator (Worman et al., 2012) that effectively functions as a low-pass filter, as described above and illustrated in Figure 4. For a given vertical offset distance, any set of κ_e and v parameters produces unique amplitude ratio and phase lag trends with respect to frequency, and if amplitude ratio and phase lag estimates can be obtained for multiple frequencies in a time-series data set, then it makes sense to seek the parameter set that best fits the frequency trends.

Given time-series records from a pair of vertically offset (Δz) thermistors, we first use cross-spectral methods to estimate coherency, amplitude ratio, and phase lag as a function of frequency, and then extract the subset of coherent, statistically independent, Ar and ϕ estimates, as described in section 3.2. In our analysis we found that Ar and ϕ varied systematically from the low end of the spectrum up to a frequency where the coherency dropped below a value of ~0.5, and we extracted this data for analysis. For each statistically independent frequency, ω_i, we then have corresponding estimates Ar_i and ϕ_i, $i = 1,2,...,N$, where N is the total number of frequency bins. These estimates represent a data vector, $\mathbf{d} = \left[Ar_1, Ar_2,...,Ar_N, \phi_1, \phi_2,...,\phi_N \right]$, of length $2N$, that will be used to estimate the model parameter(s).

We then define a vector, $\mathbf{x} = \left[\mathbf{d}, \mathbf{m} \right]^{\mathrm{T}} = \left[Ar_1, Ar_2,...,Ar_N, \phi_1, \phi_2,...,\phi_N, \mathbf{m} \right]^{\mathrm{T}}$, containing all of the observations, $\mathbf{d}$, and the model parameters, $\mathbf{m}$. We also define a covariance matrix [cov $\mathbf{x}$] for this vector, where $\left[\mathrm{cov}\ \mathbf{x} \right]_{i,i} = \sigma_{Ar_i}^2$ for $i \leq N$, and $\left[\mathrm{cov}\ \mathbf{x} \right]_{i,i} = \sigma_{\phi_i}^2 / \left(2\pi \right)^2$ for $N + 1 \leq i \leq 2N$. We quantify the uncertainties, σ_{Ar_i}, and σ_{ϕ_i}, by jackknifing the cross-spectral estimates for the individual data tapers utilized in the multi-taper method since parametric uncertainty estimates are not generally available for cross-spectral estimates (Thomson & Chave, 1991). Because the Ar and ϕ estimates are statistically independent, the uncertainties are uncorrelated and the off-diagonal elements are set to zero. The covariance matrix weights the parameter estimation process by the uncertainties, where the weight of data element d_i is proportional to the inverse of [cov $\mathbf{x}$]$_{i,i}$. The phase lag covariances are normalized by $(2\pi)^2$ to account for the difference in units/magnitudes of the amplitude ratio and phase lag estimates (dimensionless, spanning a range of 0—one for amplitude ratio, and radians, spanning a range of $-\pi$ to π for phase lag).

The final step in preparing for the parameter estimation process is to select an initial value for the model, $\mathbf{m}$. The model can either consist of κ_e (diffusion only, no flow scenario) or κ_e and v (advection-diffusion
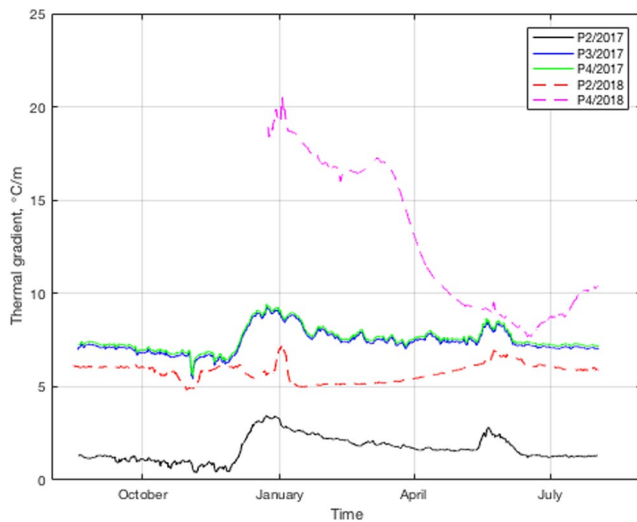
Figure 5. Thermal gradient time-series data for each deployment. Solid lines show data for the 2016–2017 deployments. Dashed lines show data for the 2017–2018 deployments.

scenario). We begin with the diffusion-only scenario because it is the simplest model, and we used an initial value of $\kappa_e = 2.0 \times 10^{-7}$ m²/s in all our analyses. The initial value of the vector, **x**, thus contains the data (amplitude ratio and phase lag estimates) along with the inital value of κ_e.

The Maximum Likelihood estimate of κ_e is then found utilizing a gradient-following approach that iteratively updates **x** until the likelihood function is maximized (Menke, 1989; Tarantola & Valette, 1982). The details of this method, including the likelihood function and the equations used to iteratively update **x**, are described in the supporting information S2. The parameter estimate statistics are characterized using the chi-square misfit of the model to the data, which measures the difference between the observed versus predicted amplitude ratio and phase lag at each frequency (see EquationS12) and the standard error of the κ_e estimate (quantified by jackknife resampling). We then rerun the method using the same data under the advection-diffusion scenario, where the model contains both the κ_e and v parameters. In our analysis we used an initial value of zero for the v parameter, and the estimate from the diffusion-only scenario for the initial value of the κ_e parameter. The chi-square misfit of the model to the data and the standard error of the model parameters are quantified as before.

The sensitivity of the data to the model parameters, and thus the precision of the parameter estimation process, is formally determined by the magnitude of the gradients, $\partial Ar / \partial m$, and $\partial \phi / \partial m$, where m is the model with parameters, κ_e, and possibly v. These gradients are a function of the vertical spacing of the thermistor pairs, frequency, and the model parameters, themselves (see Equations S10, S11, S23–S26). In general, both the amplitude ratio and phase lag are sensitive to the medium's effective thermal diffusvity, and the effective thermal diffusivity estimates can be interpreted with a high degree of confidence. Sensitivity to vertical flow rates, however, is more complex, (e.g., Hatch et al., 2006, see their Figures 3 and 4). The phase lag parameter is relatively insensitive to vertical flow, and is incapable of distinguishing between downward and upward flow directions, while the amplitude ratio is only sensitive to vertical flow over a discrete set of frequency/diffusivity/flow rate/thermistor-spacing combinations. Vertical flow rate estimates must therefore be interpreted with caution, and our method allows for the statistical significance of the velocity estimates to be assessed in two ways. First, we determine whether or not the magnitude of the parameter estimate is greater than the standard error. If not, the flow rate estimate is considered to be statistically indistinguishable from zero. If so, we then test whether or not the variance reduction achieved by including the velocity term in the inversion is significant at a specified confidence level (1σ in our analyses) using the F test. If not, we conclude that the data do not support inclusion of a flow model parameter, regardless of the parameter value. The ability to formally test the statistical significance of the fluid velocity parameter estimate in these ways represents an important advance over previous estimation methods.

4. Results

4.1. Average Thermal Gradients

Time-series records of the average vertical thermal gradient, calculated as described in section 3.1, are shown in Figure 5. Thermal gradients at the two sites near inactive pockmark fields (P3/2017, P4/2017) are nearly identical despite being offset by 1.25 km, mimicking the annual BWT cycle with values ranging from ~5 to 9 °C/m. In contrast, thermal gradients at the sites near or inside the Deep Hole thermal field, with offset distances of 60–150 m, are highly variable. The site on the eastern edge of the thermal field (P2/2017) also mimics the annual BWT cycle, but has relatively small gradients of ~1–3 °C/m. Site P2/2018, at the southern end of the active thermal field, has gradients of ~5–7 °C/m and exhibits temporal trends that are clearly influenced by, but also diverge somewhat from, the annual BWT cycle. Site P4/2018, at the
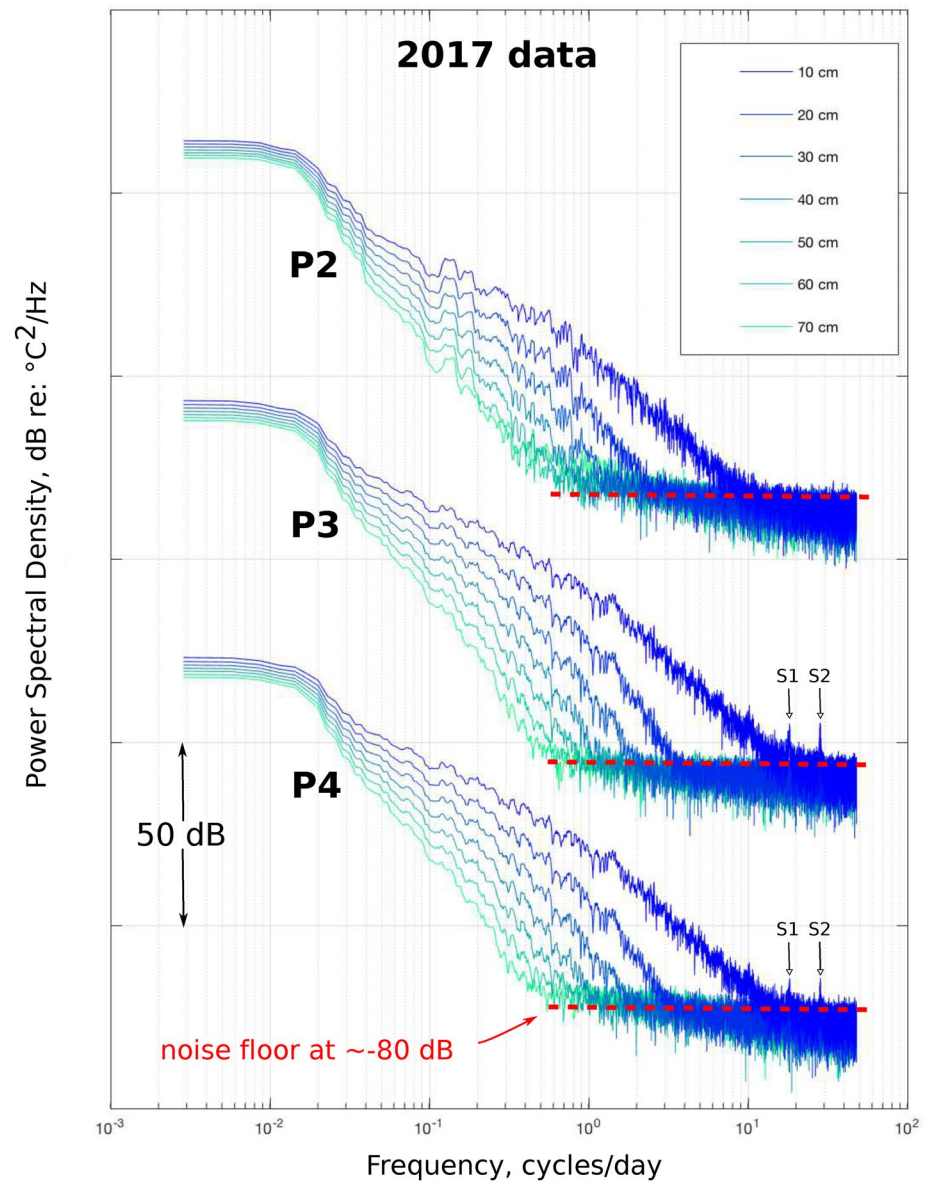
Figure 6. Power spectra for 2017 temperature time-series data shown in Figure 2. Thermistor depth shown in legend. S1 and S2 correspond to first and second mode of the lake's barotropic seiche, respectively. Noise floor at ∼−80 dB shown in red, dashed line.

northern end of the active discharge zone, has large gradients that decrease from ∼20 °C/m to ∼8 °C/m over a ∼6 months interval, with little-to-no apparent influence from the BWT cycle.

4.2. Spectral Estimates

Power spectral estimates for the raw time-series data are shown in Figures 6 and 7. The power spectra demonstrate that hydrodynamic processes in Yellowstone Lake generate a wide range of thermal signals in the shallow sediments. At the high-frequency end of the spectrum, the topmost thermistor (10 cm depth) contains signal at frequencies of up to ∼7 cycles per day (cpd) for all deployments. The topmost thermistor for the P3/2017 and P4/2017 deployments, which were not in the thermal area, contains signal from the first and second modes of the lake's barotropic seiche (Luttrell et al., 2013) at ∼18 cpd (period of ∼80 min) and ∼29 cpd (period of ∼50 min), respectively. The high-frequency content of the signals progressively
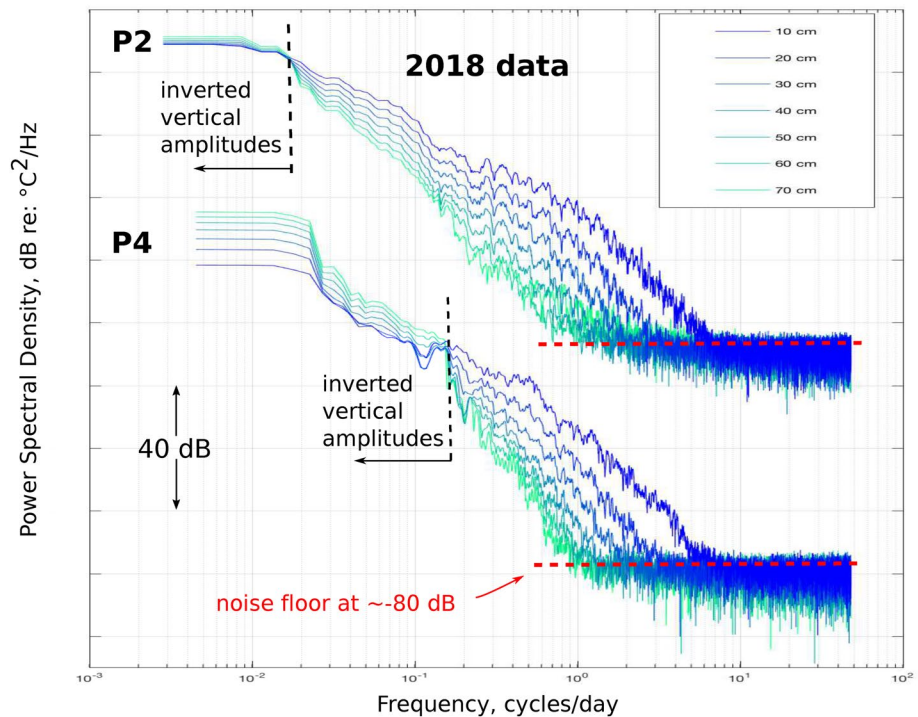
Figure 7. Power spectra for 2018 temperature time-series data shown in Figure 3. Thermistor depth shown in legend. Black, dashed vertical lines indicate frequency below which spectral levels increase, rather than decrease, with depth, indicating upward diffusion of thermal variations. Noise floor at ∼−80 dB shown in red, dashed line.

decreases with depth for all records, such that at a depth of 70 cm (i.e., the bottommost thermistor on the probes) the signal is within the noise for frequencies greater than ∼0.7 cpd (periods less than ∼34 h). The systematic decay of the thermal spectra with frequency and depth observed in the 2017 data is consistent with the downward diffusion of BWT variations at the lake floor interface (e.g., Carlslaw & Jaeger, 1959).

Spectra for the P2/2018 and P4/2018 records obtained inside the Deep Hole thermal area (Figure 7) exhibit a similar behavior to the 2017 records at the high-frequency end of the spectrum, but at low frequencies the spectral amplitudes in these records increase, rather than decrease, with depth (i.e., inverted vertical amplitudes). For the P2/2018 deployment this change in behavior is seen for frequencies less than ∼0.02 cpd (periods > 50 days), while for the P4/2018 deployment it is seen for frequencies less than ∼0.13 cpd (periods > 7.7 days). These inverted vertical amplitudes indicate that at low frequencies the spectra are dominated by upward, rather than downward, diffusing thermal signals. We thus find that sites inside the thermal area experience a combination of downward diffusion of BWT variations from the lake floor, and the upward or lateral diffusion of temperature variations associated with the hydrothermal system.

Cross-spectral estimates of the coherency, amplitude ratio, and phase lag of the thermal signals observed for each set of adjacent thermistor pairs in our VTP data are shown in Figures S1–S5 in the supporting information. The coherent subset of statistically independent amplitude ratio and phase lag estimates extracted for each time-series record are shown in Figure 8, and Figure 9, respectively. Inspection of the amplitude ratio and phase lag estimates reveals that: (1) we observe systematic amplitude ratio and phase lag relationships with respect to frequency over large bandwidths, (2) the phase lag data are generally more stable than the amplitude ratio data, presumably because they are less sensitive to fluid flow, (3) the bandwidth of coherent estimates for all sites systematically decreases with depth due to preferential attenuation of high frequencies, (4) the amplitude ratio and phase lag estimates for sites P2/2017, P3,2017, and P4/2017 are nearly identical and closely follow theoretical trends, (5) the amplitude ratio and phase lag estimates for sites P2/2018 and P4/2018 inside the active thermal area are offset to higher diffusivity trends compared to the other sites, and (6) hydrothermal processes at sites P2/2018 and P4/2018 exclude the use of low-frequency data (due
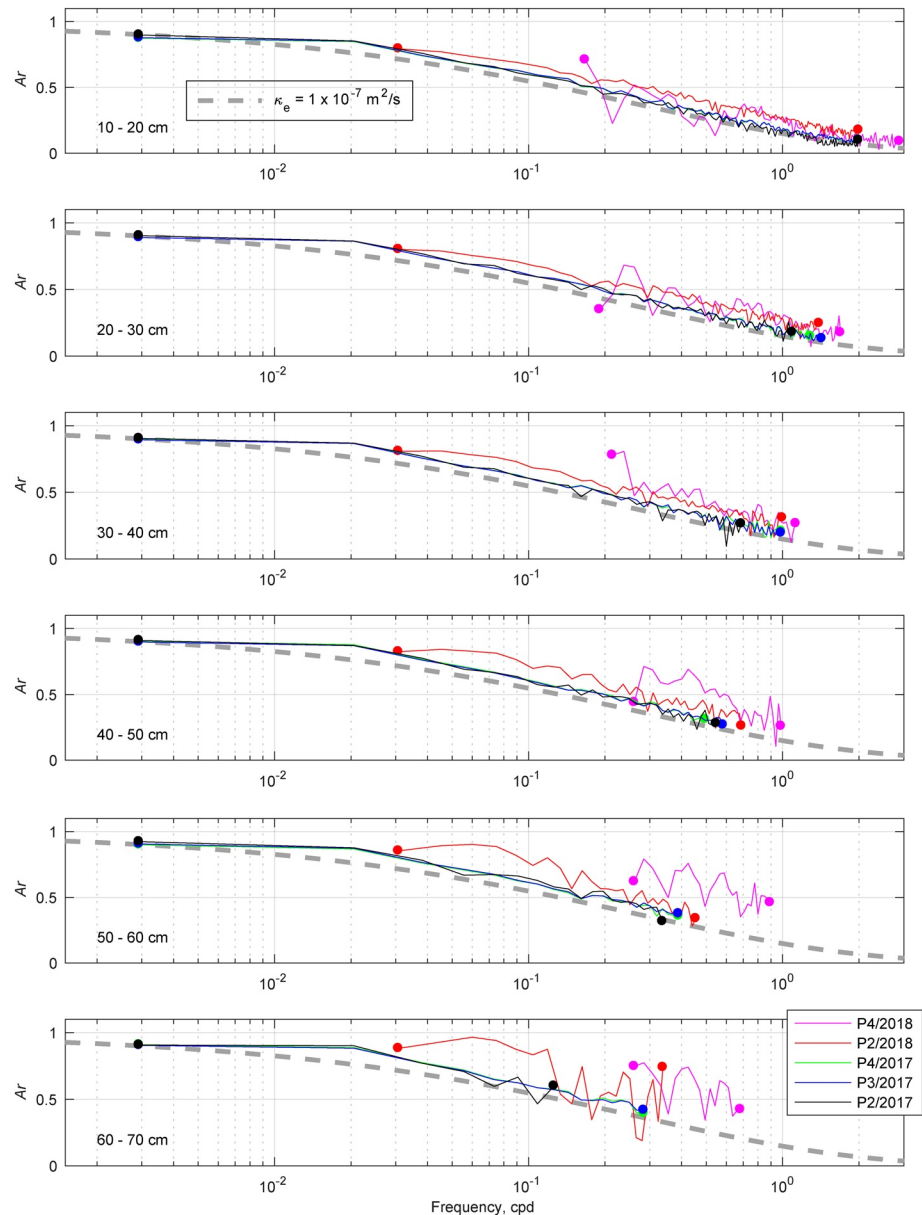
Figure 8. Cross-spectral amplitude ratio estimates for each depth interval for each VTP deployment. Colored dots indicate the upper and lower frequency limits of the coherent data used for parameter estimation. The dashed gray line shows the theoretical reference curve for $\kappa_e = 10^{-7}$ m²/s in a diffusion-only (no pore fluid flow) scenario. VTP, vertical temperature profile.

to inverted vertical amplitudes, described above) and introduce variability to the amplitude ratio trends, particularly for the deeper depth intervals.

4.3. Effective Thermal Diffusivity and Vertical Pore Fluid Velocity Parameter Estimates

The results of our multifrequency parameter estimates, including uncertainties and model misfits, are shown in Table 2. Overall, the method performed well and generated model parameter estimates that closely fit the Ar and ϕ data. The model fit to the Ar and ϕ data for each depth interval for each VTP deployment is shown in the supporting information S3. For the shallowest depth interval (10–20 cm) we have more than 200 degrees of freedom (DOFs) in the data with which to estimate either one or two model parameters, while at the deepest interval (60–70 cm) we typically have ~30 DOFs in the data. This represents a marked
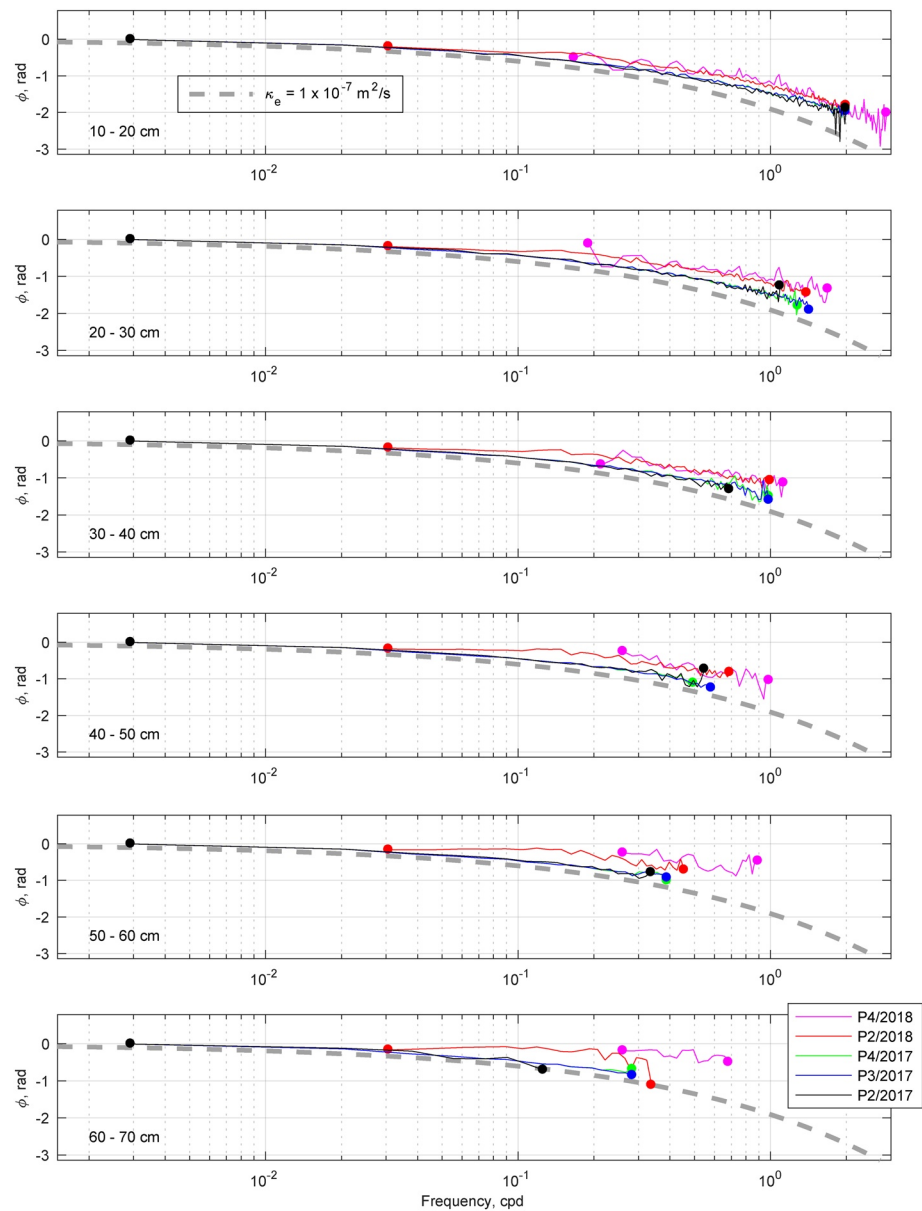
Figure 9. Cross-spectral phase lag estimates for each depth interval for each VTP deployment. Colored dots indicate the upper and lower frequency limits of the coherent data used for parameter estimation. The dashed gray line shows the theoretical reference curve for $\kappa_e = 10^{-7}$ m^2/s in a diffusion-only (no pore fluid flow) scenario. VTP, vertical temperature profile.

statistical improvement over previous approaches, where the model parameters are estimated with one or two DOFs for each discrete frequency. In general, the DOFs in the data will be determined by the nature and amplitude of the temperature variations at the water/sediment interface, along with the sampling strategy. All else being equal, the DOFs in the data, and thus the statistics of the parameter estimates, improve with: (1) increasing duration of observations, (2) decreasing sample interval, and (3) decreasing vertical spacing of thermistor pairs. This motivates the acquisition of long duration gradient data sampled as quickly as possible on closely spaced thermistors.

Our effective thermal diffusivity estimates are shown in Figure 10, and the standard errors for the estimates are shown in the Figure S11. The diffusivity estimates for all of the 2016–2017 deployments are similar and return much the same results under both (diffusion versus advection-diffusion) scenarios,

Table 2
Parameter Estimates

Depth (cm)	f_1 (cpd)	f_2 (cpd)	$\kappa_1 \pm \sigma_{\kappa 1}$ (10^{-7} m²/s)	$\kappa_2 \pm \sigma_{\kappa 2}$ (10^{-7} m²/s)	$\nu \pm \sigma_\nu$ (10^{-8} m/s)	DOF_1	X_1^2	DOF_2	X_2^2
P2/2017									
10–20	0.002	2.00	1.379 ± 0.013	1.433 ± 0.034	−11.024 ± 8.191	227	1.722	226	1.604
20–30	0.002	1.11	1.570 ± 0.018	1.571 ± 0.030	−0.243 ± 8.077	125	1.075	124	1.083
30–40	0.002	0.69	1.577 ± 0.027	1.578 ± 0.027	−0.214 ± 8.341	77	1.496	76	1.516
40–50	0.002	0.55	1.687 ± 0.061	1.659 ± 0.036	3.692 ± 12.460	63	1.658	62	1.664
50–60	0.002	0.35	1.791 ± 0.104	1.750 ± 0.055	3.863 ± 11.152	39	2.113	38	2.144
60–70	0.002	0.14	1.628 ± 0.335	1.480 ± 0.454	9.840 ± 18.610	15	1.639	14	1.719
P3/2017									
10–20	0.002	2.00	1.524 ± 0.013	1.606 ± 0.029	−20.212 ± 8.402	227	2.521	226	1.955
20–30	0.002	1.44	1.539 ± 0.011	1.565 ± 0.023	−4.799 ± 5.481	163	1.061	162	1.025
30–40	0.002	1.00	1.592 ± 0.014	1.619 ± 0.030	−3.880 ± 6.304	113	1.217	112	1.192
40–50	0.002	0.60	1.605 ± 0.025	1.607 ± 0.025	−0.279 ± 7.266	67	1.695	66	1.721
50–60	0.002	0.40	1.647 ± 0.061	1.598 ± 0.022	6.436 ± 9.685	45	2.817	44	2.717
60–70	0.002	0.30	1.612 ± 0.052	1.620 ± 0.028	−0.999 ± 6.028	33	1.965	32	2.024
P4/2017									
10–20	0.002	2.00	1.515 ± 0.016	1.602 ± 0.032	−20.105 ± 8.542	227	2.442	226	1.902
20–30	0.002	1.30	1.526 ± 0.012	1.542 ± 0.034	−2.406 ± 6.522	147	0.962	146	0.959
30–40	0.002	1.00	1.593 ± 0.021	1.609 ± 0.042	−1.954 ± 7.502	113	1.239	112	1.242
40–50	0.002	0.50	1.647 ± 0.037	1.626 ± 0.035	3.034 ± 7.819	57	1.908	56	1.912
50–60	0.002	0.40	1.655 ± 0.087	1.619 ± 0.058	3.616 ± 10.879	45	2.808	44	2.829
60–70	0.002	0.30	1.677 ± 0.069	1.678 ± 0.048	−0.151 ± 6.454	33	2.272	32	2.343
P2/2018									
10–20	0.02	2.00	2.170 ± 0.013	2.179 ± 0.016	−2.142 ± 1.909	269	0.446	268	0.445
20–30	0.02	1.40	2.480 ± 0.023	2.560 ± 0.028	−16.499 ± 4.129	187	0.667	186	0.575
30–40	0.02	1.00	2.457 ± 0.030	2.637 ± 0.068	−31.213 ± 14.520	133	0.760	132	0.612
40–50	0.02	0.70	2.952 ± 0.083	3.131 ± 0.074	−45.145 ± 15.880	91	1.034	90	0.761
50–60	0.02	0.46	2.979 ± 0.171	3.411 ± 0.235	−71.119 ± 35.841	59	1.411	58	1.138
60–70	0.02	0.34	2.800 ± 1.060	3.792 ± 1.232	−93.334 ± 82.199	43	1.865	42	1.708
P4/2018									
10–20	0.15	2.90	1.830 ± 0.045	2.083 ± 0.049	−79.079 ± 15.063	233	0.736	232	0.587
20–30	0.17	1.70	2.580 ± 0.100	2.976 ± 0.125	−83.462 ± 20.622	129	0.911	128	0.726
30–40	0.20	1.15	2.887 ± 0.136	2.931 ± 0.116	−8.610 ± 27.867	79	0.774	78	0.781
40–50	0.25	1.00	3.610 ± 0.321	3.016 ± 0.247	73.115 ± 26.942	63	0.846	62	0.768
50–60	0.25	0.90	8.674 ± 1.237	9.021 ± 1.591	−45.154 ± 66.903	55	0.995	54	0.996
60–70	0.25	0.70	12.023 ± 3.764	12.145 ± 4.360	−170.345 ± 138.645	37	2.981	36	2.762

Columns: (1) Depth interval of inversion. (2) Low end of frequency band used. (3) High end of frequency band used. (4) Diffusion-only effective thermal diffusivity estimate ± standard error. (5) Advection-diffusion effective thermal diffusivity estimate ± standard error. (6) Advection-diffusion thermal front penetration rate estimate ± standard error. (7) Degrees of freedom for diffusion-only inversion. (8) Chi-square parameter for diffusion-only inversion. (9) Degrees of freedom for advection-diffusion inversion. (10) Chi-square parameter for advection-diffusion inversion.
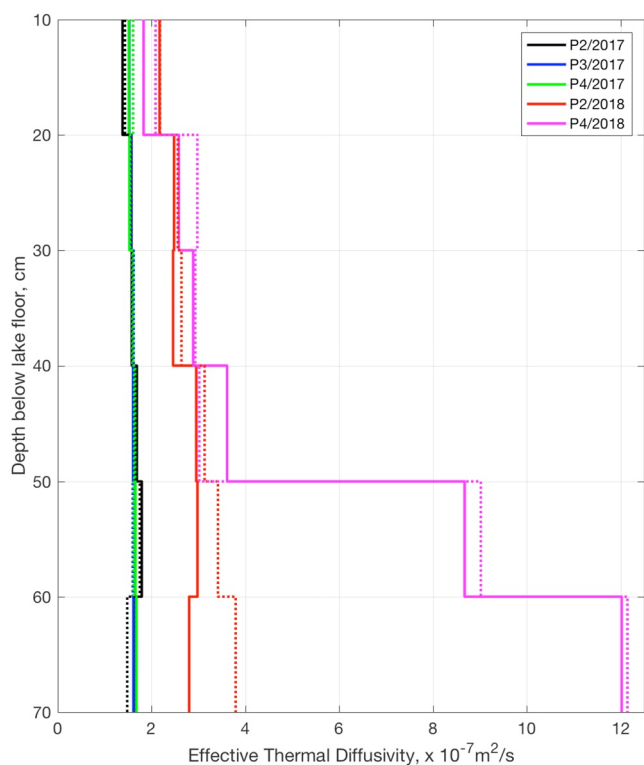
Figure 10. Effective thermal diffusivity estimates. Diffusion-only scenario results shown as solid lines. Advection-diffusion results shown as dotted lines. The step-like appearance of the plots is an artifact of the sampling and method (a separate estimate is obtained for each depth bin).

with values of $\sim 1.5 \times 10^{-7}$ m^2/s near the surface that increase slightly to $\sim 1.65 \times 10^{-7}$ m^2/s at depths of 60–70 cm. Estimates for the 2017–2018 deployments inside the Deep Hole thermal area are larger and increase more dramatically with depth, with values of $\sim 2 \times 10^{-7}$ m^2/s near the surface increasing to $\sim 3 \times 10^{-7}$ m^2/s for P2/2018, and to $\sim 12 \times 10^{-7}$ m^2/s for P4/2018 at depths of 60–70 cm. Uncertainties (standard errors) are ~ 1–2% for the shallow depth intervals, but increase to $\sim 4\%$ at the deepest depth intervals as the degrees of freedom in the inversions drop due to the progressive loss of high-frequency signal. For sites inside the thermal area, where the upward diffusion of low-frequency signals further restricts the bandwidth available for the inversions, uncertainties at the deepest depth intervals reach levels of up to ~ 20–40%. These uncertainty estimates do not include epistemic errors associated with unmodeled processes, such as three-dimensional and/or unsteady heat/mass flow, and thus should be considered as minimum values.

The advection-diffusion inversions returned estimates for the penetration rate of the thermal front, v, which is related to the vertical fluid flow rate through the ratio of sediment-to-fluid heat capacities, $v_f = v\gamma$, as described previously. We converted the thermal front penetration rate estimates to fluid flow rate estimates using matrix values appropriate for clays/muds ($\rho_m = 2.6 \times 10^3$ kg/m^3, $c_m = 780$ J/K/kg, $\rho_f = 1.0004 \times 10^3$ kg/m^3, and $c_f = 4.1991 \times 10^3$ J/K/kg). Our flow rate estimates are shown in Figure 11. Parameter estimates with magnitudes less than the standard error are considered to be statistically indistinguishable from zero, and are plotted as zero in Figure 11. Flow rate estimates that passed this first test but did not test positive as significant using the F test at the 1σ confidence level are shown as thin, solid lines in Figure 11. Flow rate estimates that passed both tests are shown as thick, solid lines in Figure 11. We find that all sites have statistically significant vertical flow rate estimates (passed both tests) within the shallowest (10–20 cm) depth interval, but only sites within the thermal area have statistically significant flow rate estimates at deeper depth intervals.

Uncertainties in the vertical fluid flow velocity estimates for sites outside the thermal area are fairly consistent and range from ~ 0.25 to 0.45 cm/day. Uncertainties for sites inside the thermal area are more variable, ranging from ~ 0.1 to 6.0 cm/day. The larger values are due to a combination of data bandwidth decreasing with depth (as with the thermal diffusivity estimates) and the considerably larger flow rate estimates obtained for the deeper depth intervals inside the thermal area (e.g., 7.3 ± 6 cm/day for P4/2018 at 60–70 cm depth). As with the thermal diffusivity uncertainties, the velocity uncertainties do not include the effects of unmodeled processes such as temporal variations and three-dimensional flow, and thus should be considered as minimum values. All of these factors, combined with the fact that the vertical fluid velocity estimate is intrinsically less sensitive to the data than the effective thermal diffusivity estimate, as noted previously, necessitate an appropriate degree of caution when interpreting the vertical fluid velocity estimates.

5. Discussion

The VTP data we acquired in Yellowstone Lake demonstrate that the thermal environment of the shallow lake floor sediments is continually changing in response to BWT variations, and, for sites inside thermal areas, hydrothermal processes, as well. To analyze the data, we developed a new method for inverting amplitude ratios and phase lags observed in the thermal data between vertically offset thermistor pairs to estimate the effective thermal diffusivity and pore fluid vertical velocity of the medium between the thermistors. Our results have implications for the thermophysical properties of the lake floor sediments, ground water-surface water exchange in deepwater locations, and the nature of discharge within the thermal area.
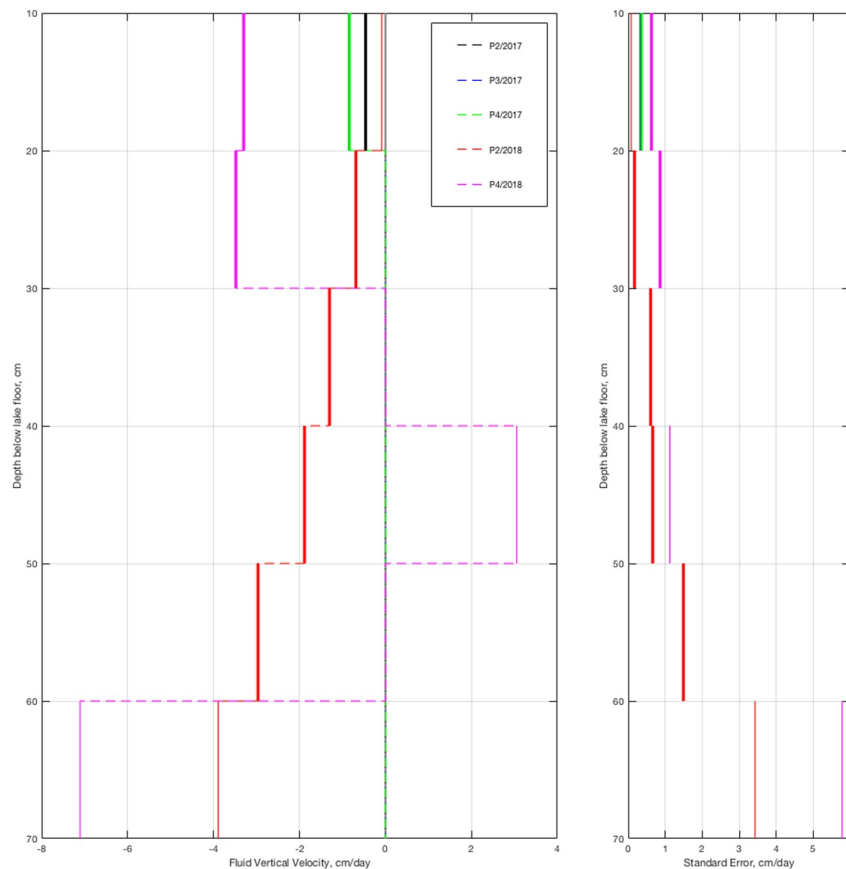
Figure 11. Advection-diffusion inversion results. Left panel: Fluid vertical velocity estimates (negative values represent upward flow). Thin solid lines shown for intervals where the standard error is less than the magnitude of the parameter estimate, but the variance reduction did not test positive for statistical significance at the 1σ level. Thick, solid lines shown intervals where the variance reduction tested positive for statistical significance at the 1σ level. Estimates statistically indistinguishable from zero plotted as zero. Right panel: Standard error for solid lines in left panel.

5.1. Cross-Spectral Parameter Estimation Method and Groundwater Fluxes

Our estimates of sediment thermal properties and vertical fluid fluxes were obtained using a new method, described in section 3.4. The key advantage of this method relative to previous approaches is that it can significantly increase the amount of information used to estimate the model parameters, which allows for statistically robust parameter estimates with formal uncertainty estimates that can be used for hypothesis testing. For example, in our shallowest (10–20 cm) depth interval we estimate two model parameters from more than 200 observational constraints, whereas previous methods (e.g., Goto et al., 2005; Hatch et al., 2006; Keery et al., 2007; Luce et al., 2013) estimate the same two parameters from two observational constraints.

The ability to quantify uncertainty is critical for the interpretation of any parameter estimate. Previous methods that generate single-frequency estimates of thermal diffusivity and/or pore fluid vertical velocity have addressed uncertainty in indirect ways since the uncertainty of the parameter estimates, themselves, is formally undefined. Recalling that methods based on the Stallman (1965) equations provide direct estimates of the "thermal front velocity," v, rather than the pore fluid velocity, v_f, in cases where assumptions about the thermal properties of the medium have been made in order to estimate the pore fluid vertical velocity, uncertainty has been assessed by considering the impact of the thermal property uncertainties on the conversion of v to v_f (e.g., Gordon et al., 2012; Keery et al., 2007). Luce et al. (2013) describe a more sophisticated approach that propagates errors in the amplitude ratio and phase lag estimates into the thermal front velocity yielded by the equations. Neither of these approaches, however, allows for the statistical significance of the model parameter estimates to be formally tested.

These statistical issues primarily pertain to interpretation of the vertical flow velocity estimates. The amplitude ratio and phase lag of a thermal signal observed between vertically offset thermistors is primarily controlled by the effective thermal diffusivity of the medium, and as our uncertainty analysis demonstrates, the diffusivity parameter estimates are robust and accurate to within a few percent. The sensitivity of the amplitude ratio and phase lag to the velocity parameter, however, is more nuanced, and it depends on both the data characteristics (oscillation frequency, thermistor spacing, sampling interval, thermistor resolution) and the magnitude and direction of the pore fluid vertical velocity (e.g., Hatch et al., 2006), and thus cannot be known *a priori*. Our method allows for the statistical significance of the velocity parameter estimate to be formally tested against the null hypothesis of no flow, and we found that many of our flow velocity estimates, including some relatively large amplitude estimates, were not significant. This underscores the fact that thermal methods will generate vertical flow velocity estimates even if the data are not sensitive to the velocity parameter, and emphasizes the importance of being able to assess the statistical significance of the velocity parameter estimates.

5.2. Sediment Thermophysical Properties

Our analyses provide in situ estimates of the thermal diffusivity of the upper 70 cm of sediments in Yellowstone Lake, including sites both inside and outside the Deep Hole thermal area. In general, we obtain different results for sites outside the thermal area compared to sites inside the thermal area. Our thermal diffusivity estimates for sites outside of the thermal area (P3/2017 and P4/2017) are remarkably consistent, increasing slightly from $\sim 1.55 \times 10^{-7}$ m^2/s in the 10–20 cm depth interval to $\sim 1.65 \times 10^{-7}$ m^2/s in the 60–70 cm depth interval. These values are slightly higher than that of water (1.4×10^{-7} m^2/s), and vary by <10% with depth, indicating that the shallow sediment at these sites is relatively homogeneous in composition and highly porous. Site P2/2017, located on the edge of the thermal area, returns similar values (Figures 10 and 11), although our diffusivity estimate for the shallowest (10–20 cm) depth interval (1.38×10^{-7} m^2/s) is marginally less than that of water—the only such estimate in our analyses. Our thermal diffusivity estimates for sites inside the Deep Hole thermal area are considerably higher than those for sites outside the thermal area, with values of $\sim 2.1 \times 10^{-7}$ m^2/s in the 10–20 cm depth interval that increase more rapidly with depth to values as high as 12.1×10^{-7} m^2/s in the 60–70 cm depth interval.

Sediments sampled outside of thermal areas in Yellowstone Lake are siliceous oozes, dominantly composed of diatoms (i.e., biogenic, amorphous silica), potassium feldspar, clays (smectite), and quartz (*Tiller*, 1995). There are no in situ diffusivity estimates from marine sites with siliceous oozes, but the mean value and standard deviation of thermal conductivity (λ) measurements from 144 siliceous sites in the Pacific Ocean is 0.780 ± 0.105 W m^{-1} K^{-1} (Stein & Abbott, 1991). Converting these values to thermal diffusivity using the relationship (Hyndman et al., 1979):

$$\kappa = \frac{\lambda}{5.79 - 3.76\lambda + 1.106\lambda^2} \left(\lambda \text{ in } Wm^{-1}K^{-1}, \text{ in } 10^{-6} m^2/s \right) \tag{4}$$

yields $2.17 \pm 0.40 \times 10^{-7}$ m^2/s. By comparison, thermal conductivity values of 0.75 ± 0.02 W m^{-1} K^{-1} were obtained for Yellowstone Lake sediments using a combination of laboratory and field studies (Morgan et al., 1977), yielding diffusivities of $2.05 \pm 0.08 \times 10^{-7}$ m^2/s using Equation 4. Both of these sets of values are slightly higher than our estimates for sites outside the Deep Hole thermal area, which may be due to length-scale/compaction factors, since the heat flow probes (Bullard, 1954) used to measure conductivity in the field penetrate the sediment to depths of several meters whereas our measurements are confined to the upper 70 cm.

Near-surface sediments sampled from Yellowstone Lake have porosities of $\sim$85–90% (Shanks et al., 2007; Tiller, 1995), similar to near-surface porosity observations for siliceous sediments in marine environments (Hamilton, 1976). Using these values, along with mixing laws established for calculating the thermal properties of aggregate sediments (e.g., Woodside & Messmer, 1961; Drury & Jessop, 1983; Goto & Matsubayashi, 2009; see supporting information S4), yields a sediment matrix (grain) diffusivity of 2.45–3.20 $\times 10^{-7}$ m^2/s for sites P3/2017 and P4/2017. Assuming there are no compositional variations in the upper 70 cm of
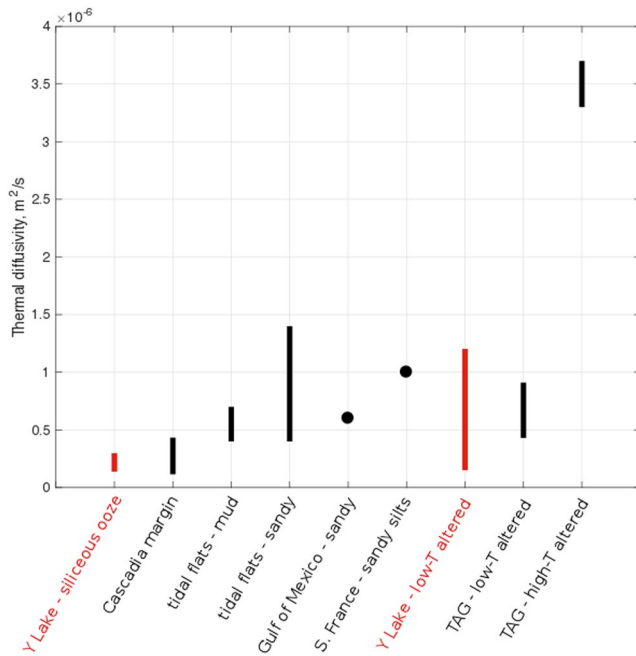
Figure 12. Comparison of in situ thermal diffusivity estimates derived from VTP time-series data. Values in red are from this study. Cascadia margin—Homola et al. (2015). Tidal flats—Thomson (2010). Gulf of Mexico—Jackson and Richardson (2000). S. France—Wheatcroft et al. (2007). TAG—Goto et al. (2002). VTP, vertical temperature profile.

sediments at these sites, the ~10% increase in diffusivity we observe with depth in these profiles corresponds to a ~10% decrease in porosity using the relationships shown in the supporting information S4.

Sediment push cores (19 cm length) from the Deep Hole thermal area are altered by hydrothermal processes, with pyrite-bearing clays largely replacing opal. These sediments are 80%–99% kaolinite by weight, with minor boehmite, pyrite, quartz, plagioclase, and smectite (Fowler, Liu, et al., 2019). The ~50% increase in thermal diffusivity that we observe in the near-surface sediments within the Deep Hole thermal area relative to sites outside the thermal area is consistent with hydrothermal alteration replacing biogenic silica with higher diffusivity clays and pyrite. Porosity data for the push cores from the Deep Hole is not available, but if we assume a similar near-surface porosity of 85–90% as for sites outside of the thermal area, then mixing laws yield a matrix diffusivity of 13–40×10^{-7} m²/s for near-surface sediments at sites P2/2018 and P4/2018. Thus, although hydrothermal alteration only increases the bulk sediment diffusivity by ~50%, it increases the matrix diffusivity by about an order of magnitude. Assuming the sediment composition inside the thermal area is constant throughout the upper 70 cm, the diffusivity profile for site P2/2018 yields a similar (~10%) porosity decrease as the sites outside the thermal area, but the diffusuvity profile for site P4/2018 yields a much larger porosity decrease of ~60%.

We are not aware of any previous estimates for the in situ thermal diffusivity of lacustrine sediments, but a small number of studies have used VTP time-series data to estimate the diffusivity of marine sediments. Homola et al. (2015) obtained estimates of 1.15×10^{-7} and 4.33×10^{-7} m²/s for two sites on the accretionary wedge of the Cascadia Margin, which is largely composed of alternating layers of pelagic clays and sandy silt turbidites. Jackson and Richardson (2000) obtained an estimate of 6×10^{-7} m²/s for sands in the northeastern Gulf of Mexico. Wheatcroft et al. (2007) obtained an estimate of 10×10^{-7} m²/s for sandy silts off the southern coast of France. Thomson (2010) obtained estimates of $4–7 \times 10^{-7}$ and $4–14 \times 10^{-7}$ m²/s for muddy, and sandy, tidal flats, respectively, in Willapa Bay (Washington, USA). Finally, Goto et al. (2002) obtained estimates of $4.3–9.1 \times 10^{-7}$ m²/s for sediments altered in a low-temperature discharge zone, and $33–37 \times 10^{-7}$ m²/s for sediments altered in a high-temperature discharge zone at the TAG hydrothermal mound on the Mid-Atlantic Ridge. The methodologies used to obtain these estimates vary, but in all cases they are based on the thermal response of shallow sediments to forcing at the seafloor interface, conceptually similar to our approach.

These in situ estimates of thermal diffusivity based on VTP time-series data are summarized in Figure 12. Our thermal diffusivity estimates for sites outside the thermal area are lower than almost all the other estimates for marine sediments, which is likely due to the low thermal diffusivity of siliceous sediments (diatoms/biogoenic silica) compared to muds (clays) and sands (quartz). Our diffusivity estimates for sites inside the Deep Hole thermal area are similar to those obtained for a low-temperature alteration site on the TAG hydrothermal mound, likely due to similarities in the alteration products (clays). Overall, we find that: (1) our thermal diffusivity estimates are broadly consistent with the composition of Yellowstone Lake sediment cores, (2) most of the observed increases in thermal diffusivity with depth are consistent with porosities decreasing from ~90% at 10 cm depth to ~80% at 70 cm depth, and (3) higher thermal diffusivities observed inside the Deep Hole thermal area are consistent with compositional changes and possibly porosity reductions associated with hydrothermal alteration (e.g., Mielke et al., 2015).

5.3. Vertical Fluid Flow Estimates

As described previously, vertical fluid velocity estimates from VTP data are less robust than effective thermal diffusivity estimates due to parameter sensitivities. Our uncertainty analysis indicates that the minimum resolvable vertical flow velocity is ~0.3 cm/day in most of our data, and somewhat larger (~1–3 cm/day)

for the deeper depth intervals at the P2/2018 and P4/2018 sites inside the Deep Hole thermal area. Here, we only interpret vertical fluid velocity estimates that test statistically significant using both the standard error test and the *F* test for variance reduction described previously.

5.3.1. Hypolentic Flow

As with our thermal diffusivity estimates, we see distinct differences in the vertical fluid flow rate estimates between sites inside and outside the thermal area. Outside the thermal area, we only obtain statistically significant pore fluid vertical velocity estimates for the shallowest (10–20 cm) depth interval, which return small (<1 cm/day), upward flow rates. Although these velocities are small, the addition of this parameter reduces the model misfit by as much as ∼25% compared to the diffusion-only scenario for these cases (Table 1), indicating that the amplitude ratio and phase lag data are being affected by processes other than diffusion. Given the high matrix porosities (85–90%) in this depth interval, and the unconsolidated nature of the surficial sediments, it seems likely that there is fluid exchange between the water column and the surficial sediments, and we consider whether this process may explain our results.

Bi-directional fluid and mass exchange within a vertically restricted zone across a sediment-water interface is an ecologically important process in streams, lakes, and marine environments, where it has been referred to as hyporheic flow, hypolentic flow, and hydrodynamic exchange, among other terms (see reviews in Huettel et al., 2014; Boano et al., 2014). Hyporheic flow can be driven by a combination of processes, including advective pumping, shear-driven flow, turbulence, wave action, tides, and diffusion (e.g., O'Connor & Harvey, 2008), and it can occur over a wide range of spatial and temporal scales (Boano et al., 2014). Most studies have focused on riverine and marine environments, which typically experience a greater range of potential forcing mechanisms compared to lakes, such that field observations of hypolentic flow in lacustrine environments are limited. We lack the observations required to quantitatively assess the potential for hypolentic flow (e.g., bottom current speeds) in Yellowstone Lake, but we do know, for example, that the lake experiences essentially continuous seiches (Luttrell et al., 2013). Seiches are capable of modulating fluid flow and seepage across a lake bed (Taniguchi & Fukuo, 1996), and the first two seiche modes of Yellowstone Lake are conspicuous in the thermal spectra at 10 cm depth for sites P3/2017 and P4/2017 (Figure 6). This suggests that the seiches are driving vertical fluid motion across the lake floor interface down to at least 10 cm depth.

The effect of hyporheic flow on heat flow in shallow sediments has been evaluated by modeling it as hydrodynamic dispersion (Bhaskar et al., 2012), which increases the effective thermal diffusivity of the medium by an amount that depends primarily on the fluid flow rate and the medium permeability (Molina-Giraldo et al., 2011). For the 2017 deployments outside the thermal area, we find that including an advective term in our inversion increases the effective thermal diffusivity estimates by ∼5% for the 10–20 cm depth interval while producing vertical flow rate estimates of ∼1 cm/day. The magnitude of these estimates are self-consistent with posited relationships between effective thermal diffusivity, flow velocities, and hydrodynamic dispersion (e.g., Bhaskar et al., 2012; Molina-Giraldo et al., 2011), but as our model does not explicitly include hypolentic flow, any such interpretations must be made with caution.

All things considered, it seems likely that seiching, and possibly other hydrodynamic processes, generates hypolentic flow within the upper ∼20 cm of the highly porous sediments on the lake bed. We observe seiche signals at a depth of 10 cm in our VTP data acquired from sites outside the thermal area, and the amplitude ratios and phase lags in our cross-spectral estimates from these sites indicate that the sediment temperatures are affected by a process other than diffusion down to a depth of ∼20 cm. Below 20 cm, we find no evidence for vertical fluid flow at these sites. Taken together, these results suggest that hypolentic flow is affecting sediment temperatures in the upper ∼20 cm of the deep Central Basin of Yellowstone Lake. Widespread hypolentic flow could have significant consequences for the mobilization and transport of solutes and nutrients in Yellowstone Lake, and this issue should be investigated further.

5.3.2. Fluid Flow Inside the Thermal Area

Vertical fluid flow velocity estimates for sites inside the thermal area are larger, more variable, and extend further into the sediment layer compared to sites outside the thermal area. For site P2/2018, we obtain statistically significant upward flow velocities that steadily increase from ∼0.7 cm/day in the 20–30 cm depth interval up ∼3 cm/day in the 50–60 cm depth interval. If the vertical fluid motion is due to buoyancy, as

may be expected inside a thermal area, then the systematic decrease in the velocity estimates as the fluids approach the lake floor interface is consistent with a decrease in buoyancy due to cooling combined with lateral spreading. Vertical flow slows to low levels and fluids begin to spread laterally once they are cooled to ambient temperatures in the highly porous sediments just below the lake floor.

For site P4/2018, we obtain statistically significant upward flow velocity estimates of ~3.4 cm/day in the 10–30 cm depth interval, which are roughly 5× the rates observed for site P2/2018. The estimates below 30 cm were highly variable but not statistically significant. The variability in the P4/2018 flow rate estimates relative to the other sites is at least partly due to the influence of hydrothermal processes, which generated upward diffusing thermal signals that limited the bandwidth of the amplitude ratio and phase lag data that could be used in the inversions. The lowest frequency used in the P4/2018 inversions is ~100× larger than the lowest frequencies used in the 2017 inversions (0.2 versus 0.002 cpd), and ~10× larger than those used in the P2/2018 inversions (0.2 versus 0.02 cpd). This loss of the low-frequency end of the spectrum, combined with a shorter record (7 months compared to 12 months for other sites) and generally noisier amplitude ratio and phase lag data (Figures 8 and 9), decreases the quality of the vertical fluid flow estimates for P4/2018 relative to the other sites. Nevertheless, our results indicate that there is upward flow of buoyant pore fluids at the P4/2018 site, with magnitudes higher than those observed/interpreted for nearby site P2/2018. It also seems likely that vertical flow velocities increase with depth, as observed for site P2/2018, due to thermal buoyancy effects, but this cannot be confirmed with our parameter estimates.

5.4. Conductive Heat Flow and Hydrothermal Circulation

We can estimate conductive heat flow, q, at each of our measurement sites by mulitplying the observed thermal gradients by the thermal conductivity, ($q = \lambda \nabla T$). As described in section 5.2, our thermal diffusivity estimates for sites outside the thermal area are consistent with the thermal conductivity estimates obtained for Yellowstone Lake sediments by Morgan et al. (1977) (0.75 ± 0.02 W m^{-1} K^{-1}). Our diffusivity estimates for sites inside the thermal area, however, are higher, and correspond to conductivity values of ~1.0 W m^{-1} K^{-1} via Equation 4 when averaged over the 10–70 cm depth interval of our observations. Using these values, we obtain the following conductive heat flow estimates (mean $\pm$ std. dev.) in units of W/m^2: P2/2017 = 1.25 $\pm$ 0.51, P3/2017 = 5.56 $\pm$ 0.48, P4/2017 = 5.67 $\pm$ 0.48, P2/2018 = 5.78 $\pm$ 0.48, P4/2018 = 12.84 $\pm$ 3.99 (Table 1).

Because our conductive heat flow estimates are proportional to the average thermal gradients, they follow the same temporal trends as the gradients (Figure 5). Heat flow at sites P2/2017, P3/2017, and P4/2017 thus correlate directly with BWT variations, with higher values when the bottom water is colder during the winter ice-covered period, and lower values during the summer months. We note that our heat flow estimates for sites P3/2017 and P4/2017 are roughly an order of magnitude greater than those obtained by Morgan et al. (1977) for nearby sites in 1974, due to higher thermal gradients. Spatial variability makes it difficult to assess the possibility of temporal variations between the 1974 and 2017 surveys, but we cannot rule out the possibility that thermal gradients at sites P3/2017 and P4/2017 increased over that ~40 years interval.

The magnitude of the thermal gradients and the temporal trends observed for the three sites in and on the edge of the thermal area (P2/2017, P2/2018, P4/2018) are remarkably different, even though the data were acquired within 100 m of each other. Site P2/2017 exhibited temporal trends associated with BWT variations, but the gradients yielded an average heat flow of 1.22 W/m^2, which is lower than the intracaldera average of 1.8 W/m^2 for the 640 ka Yellowstone caldera (Fournier et al., 1976), despite being located less than 100 m from vents actively discharging fluids at temperatures of up to 173 °C (Fowler, Tan, et al., 2019). By contrast, site P4/2018 had gradients in excess of 20 °C/m, exhibited temporal trends that were largely unrelated to BWT variations, and had spectral amplitudes that increased, rather than decreased, with depth over a wide range of frequencies. These results clearly indicate that the thermal environment at this station was primarily responding to variations due to hydrothermal processes.

The short wavelength thermal variability in both the temporal and spatial dimensions observed for sites within, and on the edge of, the Deep Hole thermal field reflect the impact of hydrothermal processes on heat flow in this area. Based on fluid chemistry and mineral alteration data, Fowler, Liu, et al. (2019) pos-

ited that the Deep Hole thermal area is driven by a steam reservoir that is trapped in the sediments by a relatively shallow, impermeable lid. In this scenario, which is supported by near-bottom magnetics data (Bouligand et al., 2020), the steam escapes the reservoir, immediately condenses, and rises to the lake floor in discrete zones. This type of flow is conceptually similar to the finger flow observed in the vadose zone of subaerial hydrologic systems (e.g., de Rooij, 2000). The partitioning of hydrothermal fluids into discrete flow fingers could result from short wavelength variability in the sediment hydraulic conductivity (e.g., Rovey & Cherkauer, 1995) flow instabilities, or a combination of both. Hydrothermal alteration modifies both the sediment composition and porosity (e.g., Mielke et al., 2015), which over time can modify the hydraulic conductivity of the medium and create preferential pathways for fluid flow. Alternatively, while finger flow is usually considered in the context of infiltration, the analysis of Wang et al. (1998) demonstrated that the instabilities that cause fingering can also occur in upward flow (seepage) environments.

Hot, upwelling flow fingers in the thermal area will create thermal halos in the neighboring sediments and generate lateral variations in sediment temperatures. It seems likely that our site P4/2018 was located in such a thermal halo. Temporal variations in the temperature of the fluids discharing at vents in the Deep Hole have been documented by Tan et al. (2020), and these variations will in turn create temporal variations in the thermal gradients of sediments within the diffusive thermal halo of the upflow zone. This kind of process provides a plausible explanation for the temporal variations in the thermal gradients observed at site P4/2018 (Figure 5). Because hydrothermal alteration changes the sediment permeability, the pathways of hydrothermal flow may change in response to an evolving permeability field. This process, which has been invoked to explain thermal variations in diffuse flow systems around deep-sea hydrothermal fields (e.g., Sohn, 2007), might also contribute to the temporal changes we observe in thermal gradients inside the thermal area.

Pore fluids within the thermal area are affected by the thermal and hydraulic perturbations associated with the flow fingers, as well as the strong thermal gradients generated by the underlying steam reservoir, and both of these factors could stimulate pore fluid convection in the sediments. Porous convection would generate zones of both upflow, with elevated thermal gradients, and downflow, with depressed thermal gradients. The anomalously low thermal gradients we observed at site P2/2017 could be thus due to recharge/infiltration of lake bottom water due to pore fluid convection at vertical velocities below the resolution limit (∼0.3 cm/day) of our data. Upflow zones of convecting pore fluids would be preferentially located next to hot fingers of hydrothermal flow, and the relatively high vertical fluid flow rate estimates obtained for site P4/2018 might be explained by this phenomenon. The convection patterns, themselves, could be unstable, depending on the Rayleigh number of the system (Lapwood, 1948), and this could also contribute to the space-time thermal variations observed in the thermal area. Our analytical method does not allow us to detect temporal variations in vertical flow velocity, but this topic could be pursued in the future.

5.5. Thermal Methods for Constraining Groundwater Flux in Lakes and Other Environments

There is a rich, and growing, literature regarding the use of thermal methods to constrain groundwater fluxes. This is largely due to the fact that thermal data are much simpler and often more economical to acquire than other approaches for constraining groundwater fluxes (e.g., seepage meters, piezometers, tracer injection experiments). The new method we present in section 3.3 has the potential to expand the hydrologic environments where thermal data may be used for groundwater studies by removing the requirement of observing and analyzing strictly diurnal thermal variations. Since any real signal can be expressed as a sum of Fourier components, any thermal perturbation that diffuses downward into a porous medium can be used to constrain groundwater fluxes, subject to the limitations regarding parameter sensitivies discussed in section 5.1.

Like Worman et al. (2012), we find that low frequencies are especially useful for constraining the model parameters because they penetrate the sediments more efficiently than high frequencies. The theoretical relationships shown in Figure 4 demonstrate that low-frequency data is especially useful for constraining upward fluxes (seepage), but frequencies lower than diurnal can still be useful for constraining downward fluxes (infiltration), depending on the medium's thermal diffusivity and the vertical thermistor spacing. These considerations motivate the acquisition of long time-series records when possible since the ability to resolve low-frequency signals depends on the record length.

Our spectral analysis demonstrates that the lake floor interface in deep portions of Yellowstone Lake experiences thermal variations over a broad spectrum of frequencies (Figures 6 and 7). Our shallowest thermistors, at a depth of 10 cm, observe signal from the low-frequency end of the spectrum (periods of 100s of days) all the way up to ~7 cpd (periods of ~3.4 h), including the first two modes of the lake's barotropic seiche. Considering that the diffusive time scale for thermal perturbations at the lake surface to penetrate to the depth of our measurement sites (>80 m) is several orders of magnitude longer than our annual observation intervals, the BWT variations we observe must be generated by hydrodynamic processes. While the hydrodynamic behavior of Yellowstone Lake has not been characterized in any detail, it is a dimictic lake that convectively overturns twice a year (Benson, 1961), it generates energetic, year-round seiches (Luttrell et al., 2013), and both these processes are clearly evident in our thermal data. In a body of water the size of Yellowstone Lake (~341 km^2), energy introduced by meteorological processes to the lake's surface (e.g., wind) can be transferred to the lake floor via a combination of barotropic and baroclinic waves and currents (e.g., Austin, 2013; Rueda et al., 2003; Wuest & Lorke, 2003), and these processes likely explain the rich thermal spectra we observe. Our data suggest that lakes, and large lakes, in particular, may be more amenable to thermal time-series methods for constraining groundwater fluxes than previously appreciated.

The observation of (barotropic) seiche periods in the thermal data from the shallow sediments supports the observation of Taniguchi and Fukuo (1996) that these seiches can modulate hypolentic flow in large lakes. A key difference between our measurements and those of Taniguchi and Fukuo (1996) is that whereas their observations were made at a site with a depth of 1.2 m, our observations were made at sites with depths > 80 m, indicating that seiches can drive hypolentic flow even in relatively deep environments. Internal (baroclinic) seiches, which are common in stratified lakes (Csanady, 1975), have also been observed to modulate heat and mass fluxes across the sediment-water interface (Bernhardt et al., 2014; Kirillin et al., 2009). Considering that seiches are ubiquitous phenomena that are also observed in semienclosed ocean harbors and basins (e.g., Arneborg & Liljebladh, 2001; Cerovecki et al., 1997; Okihiro et al., 1993), their role in driving hydrodynamic exchange between surface waters and shallow sediments is a topic that warrants further research.

6. Conclusions

Yearlong VTP data acquired from five deep sites in Yellowstone Lake provide new insight into the thermal environment of surficial sediments, the thermophysical properties of the lake sediments, and the impact of hydrothermal processes on these parameters. Our analysis of the gradient data leads to the following conclusions:

(1) Vertical temperature profiles in Yellowstone Lake surficial sediments respond to a rich spectrum of BWT variations associated with dynamic water column processes, including convective overturn and seiches, that diffuse downward into the sediments

(2) At sites in the Deep Hole thermal area, sediment temperatures also respond to hydrothermal processes

(3) At measurement sites unaffected by hydrothermal discharge, the surficial sediments have average gradients of ~7.5°C/m, consistent with their position inside the 640 ka Yellowstone Caldera, and thermal diffusivities that increase from ~1.52 × 10^{-7} m^2/s in the 10–20 cm depth interval to ~1.65 × 10^{-7} m^2/s at the 60–70 cm depth interval, consistent with a porosity decrease from ~90% to ~80% in a siliceous matrix

(4) At our measurement sites in the thermal area, the surficial sediments have highly variable thermal gradients, with average values ranging from ~1.7 °C/m to ~13 °C/m, and higher thermal diffusivities as a result of hydrothermal alteration replacing the biogenic silica with clays, quartz, and pyrite. Thermal diffusivities of ~2 × 10^{-7} m^2/s in the 10–20 cm depth interval increase to ~3 × 10^{-7} m^2/s in the 60–70 cm depth interval at one site, and to ~12 × 10^{-7} m^2/s at another. These values are consistent with near-surface porosities of ~90%, but indicate spatially variable degrees of hydrothermal alteration that can significantly reduce the matrix porosity within the upper 70 cm

(5) At sites unaffected by hydrothermal discharge, we only detect evidence for vertical fluid flow in the 10–20 cm depth interval. We interpret this as being due to hypolentic flow, which moves fluids in and out of the near-surface sediments, most likely due to hydrodynamic processes. More investigations of

this phenomenon are warranted to assess the ecological consequences of the associated nutrient and solute fluxes

(6) At sites in the Deep Hole thermal area we find evidence for spatially variable pore fluid flow, including weak (<0.3 cm/day) infiltration we attribute to convective recharge, and seepage at rates of up to ~3 cm/day we attribute to convective discharge. Temporal variations in thermal gradients at sites inside the thermal area are interpreted to result from changes in the strength and location of hot hydrothermal flow fingers on timescales as short as ~8 days.

(7) We developed and implemented a new method for estimating effective thermal diffusivities and pore fluid vertical flow rates based on VTP time-series data. The new method exploits the full spectrum of coherent variations observed in pairs of vertically offset thermistors, which significantly improves the statistical properties of the parameter estimates, and provides a means to test the significance of the vertical velocity estimates. The new method also expands the range of hydrologic environments where thermal methods may be used to constrain groundwater fluxes.

Data Availability Statement

The vertical temperature profile data reported in this paper are available through the Marine Geoscience Data System (http://doi.org/10.26022/IEDA/327524).

References

Anderson, M. P. (2005). Heat as a ground water tracer. *Ground Water*, *43*(6), 951–968. https://doi.org/10.1111/j.1745-6584.2005.00052.x

Arneborg, L., & Liljebladh, B. (2001). The internal seiches in Gullmar Fjord. Part I: Dynamics. *Journal of Physical Oceanography*, *31*, 2549–2566. https://doi.org/10.1175/1520-0485(2001)031<2549:TISIGF>2.0.CO;2

Austin, J. (2013). Observations of near-inertial energy in Lake Superior. *Limnology & Oceanography*, *58*(2), 715–728. https://doi.org/10.4391/lo.2013.58.2.071510.4319/lo.2013.58.2.0715

Balistrieri, L. S., Shanks, W. C., III, Cuhel, R. L., Aguilar, C., & Klump, J. V. (2007). The influence of sublacustrine hydrothermal vents on the geochemistry of Yellowstone Lake. In L. A. Morgan (Ed.), *Integrated Geoscience studies in the greater Yellowstone area—Volcanic, tectonic, and hydrothermal processes in the Yellowstone Geoecosystem (U. S. Geol. Surv. Prof. Pap. 1717*, pp. 169–199). Reston, VA: U. S. Geological Survey.

Bartolino, J. R., & Niswonger, R. G. (1999). Numerical simulation of vertical ground-water flux of the Rio Grande from ground-water temperature profiles, Central New Mexico.Reston, VA: U.S. Geological Survey.

Benson, N. G. (1961). *Limnology of Yellowstone Lake in relation to the cutthroat trout*. Washington DC: U.S. Government Printing Office.

Bernhardt, J., Kirillin, G., & Hupfer, M. (2014). Periodic convection within littoral lake sediments on the background of seiche-driven oxygen fluctuations. *Limnology & Oceanography*, *4*, 17–33. https://doi.org/10.1215/21573689-2683238

Bhaskar, A. S., Harvey, J. W., & Henry, E. J. (2012). Resolving hyporheic and groundwater components of streambed water flux using heat as a tracer. *Water Resources Research*, *48*, W08524. https://doi.org/10.1029/2011WR011784

Billerbeck, M., Werner, U., Polerecky, L., Walpersdorf, E., deBeer, D., & Huettel, M. (2006). Surficial and deep pore water circulation governs spatial and temporal scales of nutrient recycling in intertidal sand flat sediment. *Marine Ecology Progress Series*, *326*, 61–76. https://doi.org/10.3354/meps326061

Blume, T., Krause, S., Meinikmann, K., & Lewandowski, J. (2013). Upscaling lacustrine groundwater discharge rates by fiber-optic distributed temperature sensing. *Water Resources Research*, *49*, 7929–7944. https://doi.org/10.1002/2102WR013215

Boano, F., Harvey, J. W., Marion, A., Packman, A. I., Revelli, R., Ridolfi, L., & Wörman, A. (2014). Hyporheic flow and transport processes: Mechanisms, models, and biogeochemical implications. *Reviews of Geophysics*, *52*, 603–679. https://doi.org/10.1002/2012RG000417

Böhlke, J. K., Antweiler, R. C., Harvey, J. W., Laursen, A. E., Smith, L. K., Smith, R. L., & Voytek, M. A. (2009). Multi-scale measurements and modeling of denitrification in streams with varying flow and nitrate concentration in the upper Mississippi River basin, USA. *Biogeochemistry*, *93*(1–2), 117–141. https://doi.org/10.1007/s10533-008-9282-8

Bouligand, C., Tivey, M., Finn, C., Morgan, L. A., Pat Shanks, W. C., III, & Sohn, R. A. (2020). Geological and thermal control of the hydrothermal system in northern Yellowstone Lake: Inferences from high-resolution magnetic surveys. *Journal of Geophysical Research: Solid Earth*, *125*, e2020JB019743. https://doi.org/10.1029/2020JB019743

Bredehoeft, J. D., & Papaopulos, I. S. (1965). Rates of vertical groundwater movement estimated from the Earth's thermal profile. *Water Resources Research*, *1*(2), 325–328. https://doi.org/10.1029/wr001i002p00325

Bullard, E. C. (1945). Thermal history of the Earth. *Nature*, *156*, 35–36. https://doi.org/10.1038/156035a0

Burnett, W. C., Bokuniewicz, H., Huettel, M., Moore, W. S., & Taniguchi, M. (2003). Groundwater and pore water inputs to the coastal zone. *Biogeochemistry*, *66*, 3–33. https://doi.org/10.1023/b:biog.0000006066.21240.53

Carlslaw, H. S., & Jaeger, J. C. (1959). Conduction of heat in solids (Vol. 297). Oxford, UK: Oxford University Press.

Cartwright, K. (1970). Groundwater Discharge in the Illinois Basin as Suggested by Temperature Anomalies. *Water Resources Research*, *6*(3), 912–918. https://doi.org/10.1029/wr006i003p00912

Cerovecki, I., Orlic, M., & Hendershott, M. C. (1997). Adriatic seiche decay and energy loss to the Mediterranean. *Deep-Sea Research I*, *44*(12), 2007–2029.

Clingenpeel, S., Macur, R. E., Kan, J., Inskeep, W. P., Lovalvo, D., Varley, J., et al. (2011). Yellowstone Lake: High-energy geochemistry and rich bacterial diversity. *Environmental Microbiology*, *13*(8), 2172–2185. https://doi.org/10.1111/j.1462-2920.2011.02466.x

Constantz, J., Niswonger, R. G., & Stewart, A. E. (2008). Analysis of temperature gradients to determine stream exchanges with ground water. In *Field techniques for estimating water fluxes between surface water and ground water* (Tech. Methods Chap. 4-D2). Reston, VA: U.S. Geological Survey.

Csanady, G. T. (1967). Large-scale motion in the Great Lakes. *Journal of Geophysical Research*, *72*(16), 4151–4162. https://doi.org/10.1029/jz072i016p04151

Csanady, G. T. (1975). Hydrodynamics of large lakes. *Annual Review of Fluid Mechanics*, *7*(1), 357–386. https://doi.org/10.1146/annurev.fl.07.010175.002041

de Rooij, G. H. (2000). Modeling fingered flow of water in soils owing to wetting front instability: A review. *Journal of Hydrology*, *231–232*, 277–294. https://doi.org/10.1016/s0022-1694(00)00201-8

Drury, M. J., & Jessop, A. M. (1983). The estimation of rock thermal conductivity from mineral content; assessment of techniques. *Zentralblatt fur Geologie und Palaontologie*, *1*, 35–48.

Ferguson, S., Woodbury, A. D., & Matile, G. L. D. (2003). Estimating deep recharge rates beneath an interlobate moraine using temperature logs. *Ground Water*, *41*(5), 640–646. https://doi.org/10.1111/j.1745-6584.2003.tb02402.x

Fournier, R. O., White, D. E., & Truesdell, A. H. (1976). Convective heat flow in Yellowstone National Park. In Proceedings of the second U. N. Symposium on development and use of geothermal resources (Vol. 1, pp. 731–740). Washington, DC: U. S. Government Printing Office.

Fowler, A. P. G., Liu, Q.-l., Huang, Y., Tan, C., Volk, M. W. R., Shanks, W. C. P., III, & Seyfried, W. (2019). Pyrite δ34S and Δ33S constraints on sulfur cycling at sublacustrine hydrothermal vents in Yellowstone Lake, Wyoming, USA. *Geochimica et Cosmochimica Acta*, *265*, 148–162. https://doi.org/10.1016/j.gca.2019.09.004

Fowler, A. P. G., Tan, C., Cino, C., Scheuermann, P., Volk, M. W. R., Pat Shanks, W. C., III, & Seyfried, W. E. (2019). Vapor-driven sublacustrine vents in Yellowstone Lake, Wyoming. *Geology*, *47*(3), 223–226. https://doi.org/10.1130/G45577.1

Fuller, C. C., & Harvey, J. W. (2000). Reactive uptake of trace metals in the hyporheic zone of a mining-contaminated stream, Pinal Creek, Arizona. *Environmental Science and Technology*, *34*, 1150–1155. https://doi.org/10.1021/es990714d

Gelbrecht, J., Lengsfeld, H., Pothig, R., & Opitz, D. (2005). Temporal and spatial variation of phosphorus input, retention and loss in a small catchment of NE Germany. *Journal of Hydrology*, *304*(1–4), 151–165. https://doi.org/10.1016/j.hydrol.2004.07.028

Gordon, R. P., Lautz, L. K., Briggs, M. A., & McKenzie, J. M. (2012). Automated calculation of vertical pore-water flux from field temperature time series using the VFLUX method and computer program. *Journal of Hydrology*, *420–421*, 142–158. https://doi.org/10.1016/j.jhydrol.2011.11.053

Goto, S., Kinoshita, M., Matsubayashi, O., & Von Herzen, R. P. (2002). Geothermal constraints on the hydrological regime of the TAG active hydrothermal mound, inferred from long-term monitoring. *Earth and Planetary Science Letters*, *203*, 149–163. https://doi.org/10.1016/s0012-821x(02)00876-2

Goto, S., & Matsubayashi, O. (2009). Relations between the thermal properties and porosity of sediments in the eastern flank of the Juan de Fuca Ridge. *Earth, Planets and Space*, *61*, 863–870. https://doi.org/10.1186/bf03353197

Goto, S., Yamano, M., & Kinoshita, M. (2005). Thermal response of sediment with vertical fluid flow to periodic temperature variation at the surface. *Journal of Geophysical Research*, *110*, B01106. https://doi.org/10.1029/2004JB003419

Gurrieri, J. T., & Furniss, G. (2004). Estimation of groundwater exchange in alpine lakes using non-steady mass-balance methods. *Journal of Hydrology*, *297*, 187–208. https://doi.org/10.1016/j.jhydrol.2004.04.021

Hamilton, E. L. (1976). Variations in density and porosity with depth in deep-sea sediments. *Journal of Sedimentary Petrology*, *46*(2), 280–300.

Hatch, C. E., Fisher, A. T., Revenaugh, J. S., Constantz, J., & Ruehl, C. (2006). Quantifying surface water-groundwater interactions using time series analysis of streambed thermal records: Method development. *Water Resources Research*, *42*, W10410. https://doi.org/10.1029/2005WR004787

Hayashi, M., & Rosenberry, D. O. (2002). Effects of ground water exchange on the hydrology and ecology of surface water. *Ground Water*, *40*(3), 309–316. https://doi.org/10.1111/j.1745-6584.2002.tb02659.x

Homola, K., Johnson, H. P., & Hearn, C. (2015). In situ measurements of thermal diffusivity in sediments of the methane-rich zone of Cascadia Margin, NE Pacific Ocean. *Elementa: Science of the Anthropocene*, *3*, 000039. https://doi.org/10.12952/journal.elementa.000039

Huettel, M., Berg, P., & Kostka, J. E. (2014). Benthic exchange and biogeochemical cycling in permeable sediments. *Annual Review of Marine Science*, *6*, 23–51. https://doi.org/10.1146/annurev-marine-051413-012706

Hyndman, R. D., Davis, E. E., & Wright, J. A. (1979). The measurement of marine geothermal heat flow by a multipenetration probe with digital acoustic telemetry and insitu thermal conductivity. *Marine Geophysical Researches*, *4*, 181–205. https://doi.org/10.1007/bf00286404

Jackson, D. R., & Richardson, M. D. (2000). *Seasonal temperature gradients within a sandy seafloor: Implications for acoustic propagation and scattering*. Stennis Space Center, MS: Naval Research Lab Marine Geosciences Division. Accession ADA393656.

Kan, J., Clingenpeel, S., Macur, R. E., Inskeep, W. P., Lovalvo, D., Varley, J., et al. (2011). *Archaea* in Yellowstone Lake. *The ISME Journal*, *5*, 1784–1795. https://doi.org/10.1038/ismej.2011.56

Keery, J., Binley, A., Crook, N., & Smith, J. W. N. (2007). Temporal and spatial variability of groundwater-surface water fluxes: Development and application of an analytical method using temperature time series. *Journal of Hydrology*, *336*, 1–16. https://doi.org/10.1016/j.jhydrol.2006.12.003

Kelvin, W. T. (1863). On the Secular Cooling of the Earth. *Transactions of the Royal Society of Edinburgh*, *23*, 151–170.

Kirillin, G., Engelhardt, C., & Golosov, S. (2009). Transient convection in upper lake sediments produced by internal seiching. *Geophysical Research Letters*, *36*, L18601. https://doi.org/10.1029/2009GL040064

Klump, J. V., Remsen, C. C., & Kaster, J. L. (1988). The presence and potential impact of geothermal activity on the chemistry and biology of Yellowstone Lake, Wyoming. In M. DeLuca, & I. Babb (Eds.), *Global venting, midwater and benthic ecological processes. NOAA Symposium on Undersea Research* (pp. 81–98). Washington, DC: National Oceanic and Atmospheric Administration.

Koel, T. M., Tronstad, L. M., Arnold, J. L., Gunther, K. A., Smith, D. W., Syslo, J. M., & White, P. J. (2019). Predatory fish invasion induces within and across ecosystem effects in Yellowstone National Park. *Science Advances*, *5*, eaav1139. https://doi.org/10.1126/sciadv.aav1139

Lapwood, E. R. (1948). Convection of a fluid in a porous medium. *Mathematical Proceedings of the Cambridge Philosophical Society*, *44*(4), 508–521. https://doi.org/10.1017/s030500410002452x

Lautz, L. K. (2010). Impacts of nonideal field conditions on vertical water velocity estimates from streambed temperature time series. *Water Resources Research*, *46*, W01509. https://doi.org/10.1029/2009WR007917

Lewandowski, J., Meinikmann, K., Nützmann, G., & Rosenberry, D. O. (2015). Groundwater—The disregarded component in lake water and nutrient budgets. Part 2: Effects of groundwater on nutrients. *Hydrological Processes*, *29*(13), 2922–2955. https://doi.org/10.1002/hyp.10384

Luce, C. H., Tonina, D., Gariglio, F., & Applebee, R. (2013). Solutions for the diurnally forced advection-diffusion equation to estimate bulk fluid velocity and diffusivity in streambeds from temperature time series. *Water Resources Research*, *49*, 488–506. https://doi.org/10.1029/2012WR012380

Luttrell, K., Mencin, D., Francis, O., & Hurwitz, S. (2013). Constraints on the upper crustal magma reservoir beneath Yellowstone Caldera inferred from lake-seiche induced strain observations. *Geophysical Research Letters*, *40*, 501–506. https://doi.org/10.1002/grl.50155

Meinikmann, K., Lewandowski, J., & Nützmann, G. (2013). Lacustrine groundwater discharge: Combined determination of volumes and spatial patterns. *Journal of Hydrology*, *502*, 202–211. https://doi.org/10.1016/j.jhydrol.2013.08.021

Menke, W. (1989). *Geophysical data analysis: Discrete inverse theory. International Geophysics Series*. Cambridge, MA: Academic Press.

Mielke, P., Nehler, M., Bignall, G., & Sass, I. (2015). Thermo-physical rock properties and the impact of advancing hydrothermal alteration—A case study from the Tauhara geothermal field, New Zealand. *Journal of Volcanology and Geothermal Research*, *301*, 14–28. https://doi.org/10.1016/j.volgeores.2015.04.007

Molina-Giraldo, N., Bayer, P., & Blum, P. (2011). Evaluating the influence of thermal dispersion on temperature plumes from geothermal systems using analytical solutions. *International Journal of Thermal Sciences*, *50*, 1223–1231. https://doi.org/10.1016/j.ijthermalsci.2011.02.004

Morgan, L. A., Shanks, W. C., III, Lovalvo, D. A., Johnson, S. Y., Stephenson, W. J., Pierce, K. L., et al. (2003). Exploration and discovery in Yellowstone Lake: Results from high-resolution sonar imaging, seismic reflection profiling, and submersible studies. *Journal of Volcanology and Geothermal Research*, *122*, 221–242. https://doi.org/10.1016/S0377-0273(02)00503-6

Morgan, P., Blackwell, D. D., Spafford, R. E., & Smith, R. B. (1977). Heat flow measurements in yellowstone lake and the thermal structure of the Yellowstone Caldera. *Journal of Geophysical Research*, *82*(26), 3719–3732. https://doi.org/10.1029/jb082i026p03719

Mortimer, C. H. (1941). The exchange of dissolved substances between mud and water in Lakes. *Journal of Ecology*, *29*(2), 280–329. https://doi.org/10.2307/2256395

Mulholland, P. J., Fellows, C. S., Tank, J. L., Grimm, N. B., Webster, J. R., Hamilton, S. K., et al. (2001). Inter-biome comparison of factors controlling stream metabolism. *Freshwater Biology*, *46*, 1503–1517. https://doi.org/10.1046/j.1365-2427.2001.00773.x

O'Connor, B. L., & Harvey, J. W. (2008). Scaling hyporheic exchange and its influence on biogeochemical reactions in aquatic ecosystems. *Water Resources Research*, *44*, W12423. https://doi.org/10.1029/2008WR007160

Okihiro, M., Guza, R. T., & Seymour, R. J. (1993). Excitation of seiche observed in a small harbor. *Journal of Geophysical Research*, *98*(C10), 18201–18211. https://doi.org/10.1029/93jc01760

Percival, D. B., & Walden, A. T. (1993). *Spectral analysis for physical applications*. Cambridge, UK:Cambridge University Press.

Precht, E., & Huettel, M. (2004). Rapid wave-driven advective pore water exchange in a permeable coastal sediment. *Journal of Sea Research*, *51*, 93–107. https://doi.org/10.1016/j.seares.2003.07.003

Rosenberry, D. O. (2000). Unsaturated-zone wedge beneath a large, natural lake. *Water Resources Research*, *36*, 3401–3409. https://doi.org/10.1029/2000WR900213

Rosenberry, D. O., Lewandowski, J., Meinikmann, K., & Nützmann, G. (2015). Groundwater—The disregarded component in lake water and nutrient budgets. Part 1: Effects of groundwater on hydrology. *Hydrological Processes*, *29*(13), 2895–2921. https://doi.org/10.1002/hyp.10403

Rovey, C. W., II, & Cherkauer, D. S. (1995). Scale dependency of hydraulic conductivity measurements. *Ground Water*, *33*(5), 769–780. https://doi.org/10.1111/j.1745-6584.1995.tb00023.x

Rueda, F. J., Schladow, S. G., & Palmarsson, S. O. (2003). Basin-scale internal wave dynamics during a winter cooling period in a large lake. *Journal of Geophysical Research*, *108*(C3), 3097. https://doi.org/10.1029/2001JC000942

Sebok, E., Duque, C., Kazmierczak, J., Engesgaard, P., Nilsson, B., Karan, S., & Frandsen, M. (2013). High-resolution distributed temperature sensing to detect seasonal groundwater discharge into Lake Vaeng, Denmark. *Water Resources Research*, *49*, 5355–5368. https://doi.org/10.1002/wrcr.20436

Shanks, W. C., III, Alt, J. C., & Morgan, L. A. (2007). Geochemistry of sublacustrine hydrothermal deposits in yellowstone lake—Hydrothermal reactions, stable-isotope systematics, sinter deposition, and spire formation. Reston, VA:U.S. Geological Survey.

Sierszen, M. E., Hrabik, T. R., Stockwell, J. D., Cotter, A. M., Hoffman, J. C., & Yule, D. L. (2014). Depth gradients in food-web processes linking habitats in large lakes: Lake Superior as an exemplar ecosystem. *Freshwater Biology*, *59*, 2122–2136. https://doi.org/10.1111/fwb.12415

Sohn, R. A. (2007). Stochastic analysis of exit fluid temperature records from the active TAG hydrothermal mound (Mid-Atlantic Ridge, 26°N): 1. Modes of variability and implications for subsurface flow. *Journal of Geophysical Research*, *112*, B07101. https://doi.org/10.1029/2006JB004435

Sohn, R. A., Harris, R., Linder, C., Luttrell, K., Lovalvo, D., Morgan, L., et al. (2017). Exploring the restless floor of Yellowstone Lake. *Eos*, *98*. https://doi.org/10.1029/2017EO087035

Sohn, R. A., Luttrell, K., Shroyer, E., Stranne, C., Harris, R. N., & Favorito, J. E. (2019). Observations and Modeling of a Hydrothermal Plume in Yellowstone Lake. *Geophysical Research Letters*, *46*. https://doi.org/10.1029/2019gl082523. https://doi.org/10.1029/2019GL082523

Sorey, M. L. (1971). Measurement of vertical groundwater velocity from temperature profiles in wells. *Water Resources Research*, *7*(4), 963–970. https://doi.org/10.1029/wr007i004p00963

Stallman, R. W. (1965). Steady one-dimensional fluid flow in a semi-infinite porous medium with sinusoidal surface temperature. *Journal of Geophysical Research*, *70*, 2821–2827. https://doi.org/10.1029/jz070i012p02821

Stein, C. A., & Abbott, D. H. (1991). Implications of estimated and measured thermal conductivity for oceanic heat flow studies. *Marine Geophysical Researches*, *13*, 311–329. https://doi.org/10.1007/bf00366281

Stets, E. G., Winter, T. C., Rosenberry, D. O., & Striegl, R. G. (2010). Quantification of surface water and groundwater flows to open- and closed-basin lakes in a headwaters watershed using a descriptive oxygen stable isotope model. *Water Resources Research*, *46*, W03515. https://doi.org/10.1029/2009WR007793

Suzuki, S. (1960). Percolation measurements based on heat flow through soil with special reference to paddy fields. *Journal of Geophysical Research*, *65*(9), 2883–2885. https://doi.org/10.1029/jz065i009p02883

Tan, C., Fowler, A. P. G., Tudor, A., & Seyfried, W. E. (2020). Heat and mass transport in sublacustrine vents in Yellowstone Lake, Wyoming: In-situ chemical and temperature data documenting a dynamic hydrothermal system. *Journal of Volcanology and Geothermal Research*, *405*, 107043. https://doi.org/10.1016/j.volgeores.2020.107043

Taniguchi, M. (1993). Evaluation of vertical groundwater fluxes and thermal properties of aquifers based on transient temperature-depth profiles. *Water Resources Research*, *29*(7), 2021–2026. https://doi.org/10.1029/93WR00541

Taniguchi, M., & Fukuo, Y. (1996). An effect of seiche on groundwater seepage rate into Lake Biwa, Japan. *Water Resources Research*, *32*(2), 333–338. https://doi.org/10.1029/95WR03245

Tarantola, A., & Valette, B. (1982). Generalized nonlinear inverse problems solved using the least squares criterion. *Reviews of Geophysics*, *20*(2), 219–232. https://doi.org/10.1029/rg020i002p00219

Thomson, D. J. (1982). Spectrum estimation and harmonic analysis. *Proceedings of the IEEE*, *70*, 1055–1096. https://doi.org/10.1109/proc.1982.12433

Thomson, D. J., & Chave, A. D. (1991). Jackknife error estimates for spectra, coherences, and transfer functions. In S. Haykin (Ed.), Advances in spectral analysis and Array processing (Vol. 1, pp. 58–113). Upper Saddle River, NJ: Prentice Hall.

Thomson, J. (2010). Observations of thermal diffusivity and a relation to the porosity of tidal flat sediments. *Journal of Geophysical Research*, *115*, C05016. https://doi.org/10.1029/2009JC005968

Tiller, C. C. (1995). *Postglacial sediment stratigraphy of large lakes in Greater Yellowstone: Scenarios of tectonic and climatic forcing* (PhD dissertation). Minneapolis, MN:University of Minnesota.

Tristram, D. A., Krause, S., Levy, A., Robinson, Z. P., Waller, R. I., & Weatherill, J. J. (2015). Identifying spatial and temporal dynamics of proglacial groundwater-surface-water exchange using combined temperature-tracing methods. *Freshwater Science*, *34*(1), 99–110. https://doi.org/10.1086/679757

Wang, Z., Feyen, J., & Elrick, D. E. (1998). Prediction of fingering in porous media. *Water Resources Research*, *34*(9), 2183–2190. https://doi.org/10.1029/98wr01472

Wheatcroft, R. A., Stevens, A. W., & Johnson, R. V. (2007). In situ time-series measurements of subseafloor sediment properties. *IEEE Journal of Oceanic Engineering*, *32*(4), 862–871. https://doi.org/10.1109/joe.2007.907927

Wilson, A. M., Woodward, G. L., & Savidge, W. B. (2016). Using heat as a tracer to estimate the depth of rapid porewater advection below the sediment-water interface. *Journal of Hydrology*, *538*, 743–753. http://doi.org/10.1016/j.hydrol.2016.04.047

Winter, T. C. (1981). Uncertainties in estimating the water balance of lakes. *Journal of American Water Resources Association*, *17*(1), 82–115. https://doi.org/10.1111/j.1752-1688.1981.tb02593.x

Winter, T. C. (1983). The interaction of lakes with variably saturated porous media. *Water Resources Research*, *19*(5), 1203–1218. https://doi.org/10.1029/wr019i005p01203

Winter, T. C. (1999). Relation of streams, lakes, and wetlands to groundwater flow systems. *Hydrogeology Journal*, *7*, 28–45. https://doi.org/10.1007/s100400050178

Woodside, W., & Messmer, J. H. Thermal conductivity of porous media. I: Unconsolidated sands. *Journal of Applied Physics*, *32*, 1688–1699. https://doi.org/10.1063/1.1728419

Worman, A., Riml, J., Schmadel, N., Neilson, B. T., Bottacin-Busolin, A.,& Heavilin, J. E. (2012), Spectral scaling of heat fluxes in streambed sediments, *Geophysical Research Letters*, *39*, L23402. https://doi.org/10.1029/2012GL053922

Wuest, A., & Lorke, A. (2003). Small-scale hydrodynamics in lakes. *Annual Review of Fluid Mechanics*, *35*, 373–412. https://doi.org/10.1146/annurev.fluid.35.101101.161220